View metadata, citation and similar papers at core.ac.uk
brought to you by CORE
provided by Woods Hole Open Access Server

A mechanistic model of mid-latitude decadal climate variability

S. Kravtsov *,1

Department of Mathematical Sciences, University of Wisconsin-Milwaukee, P.O. Box 413, Milwaukee, WI 53201; Phone: 414-229-4934; Fax: 414-229-4907

W. K. Dewar

Department of Oceanography, Florida State University, Tallahassee, FL 32306-3048

M. Ghil

Department of Atmospheric and Oceanic Sciences and Institute of Geophysics and Planetary Physics, University of California-Los Angeles, Los Angeles, CA 90095 and Département Terre–Atmosphère–Océan and Laboratoire de Météorologie Dynamique (CNRS and IPSL), Ecole Normale Supérieure, Paris

J. C. McWilliams

Department of Atmospheric and Oceanic Sciences and Institute of Geophysics and Planetary Physics, University of California-Los Angeles, Los Angeles, CA 90095

P. Berloff

Physical Oceanography Department, Woods Hole Oceanographic Institute, Woods Hole, MA 02543

Preprint submitted to Elsevier Science *8 August 2007*

Abstract

A simple heuristic model of coupled decadal ocean–atmosphere modes in middle latitudes is developed. Previous studies have treated atmospheric intrinsic variability as a linear stochastic process modified by a deterministic coupling to the ocean. The present paper takes an alternative view: based on observational, as well as process modeling results, it represents this variability in terms of irregular transitions between two anomalously persistent, high-latitude and low-latitude jet-stream states. Atmospheric behavior is thus governed by an equation analogous to that describing the trajectory of a particle in a double-well potential, subject to stochastic forcing. Oceanic adjustment to a positional shift in the atmospheric jet involves persistent circulation anomalies maintained by the action of baroclinic eddies; this process is parameterized in the model as a delayed oceanic response. The associated sea-surface temperature anomalies provide heat fluxes that affect atmospheric circulation by modifying the shape of the double-well potential. If the latter coupling is strong enough, the model's spectrum exhibits a peak at a periodicity related to the ocean's eddy-driven adjustment time. A nearly analytical approximation of the coupled model is used to study the sensitivity of this behavior to key model parameters.

Key words: coupled climate variability, stochastic models, double-well potential

* Corresponding author
Email address: kravtsov@uwm.edu (S. Kravtsov).
[1] *Additional affiliation:* Department of Atmospheric and Oceanic Sciences and Institute of Geophysics and Planetary Physics, University of California-Los Angeles, Los Angeles, CA 90095

1 Introduction

Observations (Deser and Blackmon 1993; Kushnir 1994; Czaja and Marshall 2001) and general circulation models (GCMs) [Grötzner et al. 1998; Rodwell et al. 1999; Mehta et al. 2000] have provided evidence for coupled decadal variability of the mid-latitude North Atlantic ocean–atmosphere system. Conceptual models suggest explanations for this variability in terms of a delayed ocean response to a noisy atmospheric forcing associated with the North Atlantic Oscillation (NAO; Hurrell 1995). The NAO is an atmospheric mode that has a coherent spatial pattern (Hurrell et al. 2003) and a time dependence that contains a large stochastic component (Wunsch 1999). The proposed delays have been related to a variety of ocean processes; examples include mean ocean advection (Saravanan and McWilliams 1998) or planetary wave propagation (Jin 1997; Neelin and Weng 1999; Czaja and Marshall 2001). Coupling can amplify the linear modes associated with the above physical processes and imprint the slow time scales onto the NAO variability (Marshall et al. 2000). Alternative explanations identified oceanic nonlinearity as a possible source of the oscillatory behavior (Jiang et al. 1995; Cessi 2000; Dewar 2001; Dijkstra and Ghil 2005; Simonnet et al. 2006). Dewar (2001), in particular, argued for a key role of intrinsic oceanic, eddy-driven variability in controling the spectral content of the coupled system at decadal and longer time scales.

Many of the theoretical results mentioned above depend in a crucial way on the formulation of a sea-surface temperature (SST) feedback on the atmospheric NAO. The sign, magnitude, and spatial pattern of this feedback inferred from GCM results is, however, controversial; compare, for example, Peng et al. (1995, 1997) and Kushnir and Held (1996). In general, the linear response

of the atmospheric circulation to SST anomalies associated with mid-latitude variability is weak; see, however, Feliks et al. (2004, 2007).

Kravtsov et al. (2006b, 2007a), in their idealized quasi-geostrophic (QG) ocean–atmosphere model, have recently identified a novel type of coupled behavior in which atmospheric nonlinearity plays a key role. In particular, ocean-induced SST anomalies affected the occupation frequency of two distinct atmospheric regimes associated with the extreme phases of the NAO. The objective of the present paper is to develop a simple conceptual model of this coupled phenomenon.

The paper is organized as follows. In section 2, we review the dynamics of the decadal coupled mode in Kravtsov et al. (2006b, 2007a). A conceptual model which incorporates the essential ingredients of this coupled behavior is developed and analyzed in section 3. In section 4 we introduce further model simplifications that make the problem analytically tractable, and analyze the sensitivity of the coupled variability to parameters. Concluding remarks follow in section 5.

2 Review of coupled variability in the QG model

We provide here a brief description of the Kravtsov et al.'s (2006b, 2007a) coupled QG model and refer the reader to Kravtsov et al. (2007a) for the complete model formulation. The model consists of a closed rectangular ocean basin and an overlying atmospheric channel on a β-plane. This configuration mimics, in an idealized fashion, the coupled ocean–atmosphere system comprised of the North Atlantic basin and the mid-latitude atmosphere above

it and extending further up- and downstream. The model components have three layers in the ocean and two layers in the atmosphere, and are coupled via a simple ocean mixed-layer model with a diagnostic momentum closure and nonlinear SST advection. Both oceanic and atmospheric components are placed in a highly nonlinear regime characterized by vigorous intrinsic variability. This is achieved by choosing the oceanic horizontal resolution to be 10 km and the oceanic horizontal viscosity to be 200 $m^2\ s^{-1}$. The atmospheric horizontal resolution is 160 km and the horizontal super-viscosity is chosen to be $-1.6 \times 10^{16}\ m^2\ s^{-1}$.

The ocean circulation is driven by the wind and (along with Ekman currents) advects SST , which, in turn, affects the atmospheric circulation by modifying ocean–atmosphere heat exchange at the boundary separating the two fluids. All the vertical heat fluxes are parameterized as functions of SST and atmospheric temperature using standard linear approximations for radiative fluxes and bulk formulas for ocean–atmosphere heat exchange. The atmospheric temperature that enters the radiation/heat exchange formulas is assumed to be linearly related to the instantaneous height of the interface dividing the two atmospheric layers. The atmospheric heat gain per unit time is being converted into the entrainment mass fluxes between the two atmospheric layers, which directly enters the equation for baroclinic QG streamfunction (this quantity is proportional to atmospheric interface displacement). The heat exchange with the mixed layer affects the ocean QG interior in the same fashion, as the entrainment of fluid between two uppermost oceanic layers; the base-of-the-mixed layer entrainment heat fluxes being computed via McDougall and Dewar (1998) parameterization.

2.1 Atmospheric climate

The leading stationary mode of the coupled model's atmospheric variability is shown in Fig. 1 in terms of the corresponding empirical orthogonal function (EOF; Preisendorfer 1988) of the Ekman pumping w_{E}. This mode (Fig. 1a) is associated with irregular shifts of the model's mid-latitude atmospheric jet north and south of its time-mean position (Fig. 1b). The corresponding probability density function (PDF; not shown) is skewed, with the main peak near the location of the dominant high-latitude atmospheric state, and a secondary shoulder indicative of the presence of the less occupied low-latitude state. This nongaussianity is an intrinsic nonlinear atmospheric phenomenon, as it is present in uncoupled, atmosphere-only simulations (Kravtsov et al. 2005a). It may also characterize some of the observed atmospheric variability in the Northern Hemisphere (Kravtsov et al. 2006a), although these results are still a subject of ongoing scientific debate (see section 5.2).

2.2 Oceanic climate: Role of eddies

The climatology of oceanic upper-layer transport is shown in Fig. 2. The ocean circulation exhibits a classical double-gyre pattern in the northern part of the basin (Dijkstra and Ghil 2005), as well as an additional weaker gyre in the south (Fig. 2a). Oceanic variability (see below) is strongest in the region of the intense and narrow eastward jet which forms at the confluence of two western boundary currents; this region is marked by a heavy solid contour in Fig. 2a and will now be considered in greater detail.

Ocean eddies play an important role in maintaining the eastward jet. Let us

decompose the upper-layer streamfunction Ψ_1 as

$$\begin{aligned}\Psi_1 &= \overline{\Psi}_1 + \Psi'_1, \\ \Psi'_1 &= \Psi'_{1,\mathrm{L}} + \Psi'_{1,\mathrm{H}}.\end{aligned} \tag{1}$$

Here the bar denotes the time mean, while the prime denotes the deviations from the time mean; the subscripts L and H refer to the low-pass and high-pass filtered (Otnes and Enochson 1978) variations of the streamfunction; the cut-off frequency that separates L from H is 1/2 year^{-1}. Let us also define the upper-layer potential vorticity Q_1 as

$$Q_1 = \nabla^2 \Psi_1 + \frac{f_0^2}{g' H}(\Psi_2 - \Psi_1), \tag{2}$$

where Ψ_2 is the middle-layer streamfunction, f_0 is the Coriolis parameter, g' is the reduced gravity, and H is the unperturbed depth of the upper layer. The quantities Ψ_2 and Q_1 are also decomposed, in analogy with Eq. (1), into the time mean, as well as low- and high-pass filtered components.

If the Jacobian operator is defined as usual, by $J(\Psi,\, Q) \equiv \Psi_x Q_y - \Psi_y Q_x$, the tendency $\partial Q'_1/\partial t$ of the upper-layer, transient potential vorticity is given by

$$\begin{aligned}\partial Q'_1/\partial t = &- J(\Psi'_{1,\mathrm{H}},\, Q'_{1,\mathrm{H}}) - J(\Psi'_{1,\mathrm{L}},\, Q'_{1,\mathrm{L}}) \\ &- [J(\Psi'_{1,\mathrm{H}},\, Q'_{1,\mathrm{L}}) + J(\Psi'_{1,\mathrm{L}},\, Q'_{1,\mathrm{H}})] + \ \ [\text{linear} \ \ \text{terms}];\end{aligned} \tag{3}$$

analogous expressions hold for the other two layers. The streamfunction tendency $\partial \Psi'_1/\partial t$ (multiplied by the thickness H of the upper layer) associated with the time-mean eddy forcing due to the sum of the nonlinear terms in Eq. (3) is shown, for the eastward-jet region, in Fig. 2b, while the analogous quantity due to the first and second nonlinear terms in Eq. (3) is displayed in Figs. 2c and 2d, respectively; the tendencies due to cross-frequency term are much

smaller and not shown. Note that high-frequency (Fig. 2c) and low-frequency (Fig. 2d) eddy tendencies have a similar dipolar pattern and are comparable in magnitude near the western boundary. The high-frequency eddies, however, dominate maintenance of the eastward jet extension in the interior of the ocean, as represented by a relatively weak tendency dipole of the opposite sign and to the east of the main dipole, located close to the western boundary; the weaker, secondary dipole extends all the way to the eastern boundary of the inertial recirculation region shown in Figs. 2b,c.

The decomposition (1) uses a simple statistical time filtering to isolate the baroclinic eddies. A more dynamically consistent decomposition was developed by Berloff (2005a,b) to show that the high-frequency eddies help maintain the eastward-jet extension via a nonlinear rectification process. These eddies do so by supplying the potential vorticity anomalies that are then preferentially deposited as positive anomalies to the north of the jet and negative anomalies to the south, thereby forcing an intensified jet; the anomaly-sign selection is carried out by the combined action of β-effect and nonlinearity (Berloff 2005c). Berloff et al. (2007) have shown how this process plays a central role in the coupled model's dynamics. One manifestation of this dynamics is the coupled oscillatory mode discussed next.

Figure 3 shows the upper-ocean streamfunction (contours) and ocean eddy forcing (color levels) regressed, at various lags, onto the leading EOF of Ψ_1; once again, only the eastward-jet portion of the ocean basin is displayed. In the course of the variability illustrated herewith, the ocean's subtropical and subpolar gyres change in phase opposition, along with the intensity of the eastward jet that separates them: at lag 0 the subtropical gyre is large and the eastward jet is intense, while at lags $\pm$10 years the subtropical gyre shrinks and

the jet becomes weaker. The associated SST anomalies (not shown) have spatial patterns similar to those of the streamfunction anomalies, with a tongue of positive SST anomalies in the eastward-jet region at lag 0 and negative anomalies at lags ± 10 years.

One can show that this mode is due largely (but not solely; see the next paragraph and section 2c) to the forced response of the ocean to the atmospheric jet-shifting mode (Fig. 1). To do so, we have first conducted a long atmospheric simulation forced by the ocean climatology from the coupled run; the character and amplitude of atmospheric variability in this simulation was very similar to that in the coupled run. We then performed two ocean-only simulations, both forced by histories developed from this uncoupled atmospheric run. In the first case, the full history was used, and the leading mode of oceanic variability (not shown) was very similar to that of Fig. 3. The second simulation employed the atmospheric history consisting of the full atmospheric history minus the jet shifting behavior; that is, the jet-shifting EOF was subtracted from the atmospheric evolution. In the latter simulation, the ocean variability was very different from the coupled run's variability, and the mode shown in Fig. 3 was not found among the significant EOFs.

The coupled model's variability has a preferred time scale of about 20 years, suggesting that the oceanic processes controling the SST anomalies introduce a weak periodicity into otherwise irregular atmospheric-jet transitions. The high-frequency ocean eddy interactions, once again, maintain the ocean circulation anomalies in Fig. 3 and are thus a dominant contribution to the coupled variability. A coupled model with a coarse-resolution, high-viscosity ocean, in which the eddies are largely damped (not shown), does not support the coupled mode found in the eddy-rich case being discussed.

2.3 Dynamics of the coupled mode

The Fourier spectra of the atmospheric jet-shifting mode and ocean kinetic energy from an 800-year-long simulation of the coupled model are shown in Fig. 4a. Both spectra are characterized by enhanced power in the interdecadal band and are thus consistent with Fig. 3. More advanced spectral methods (Ghil et al. 2002) actually exhibit a broad spectral peak centered at 21 years (not shown). Fig. 4b shows the squared coherence spectrum (Timmermann et al. 1998) of the the atmospheric jet position and oceanic kinetic energy. This spectrum also exhibits a broad peak at a bi-decadal period, which indicates increased synchronization between the ocean and atmosphere at these frequencies and thus suggests a coupled phenomenon.

We have used a number of different metrics to characterize this coupled variability. An example is shown in Fig. 5a, which shows cross-correlations between the annual upper ocean heat content time series and a measure of atmospheric variability, at various lags. The particular atmospheric quantity used here was the occupation frequency of the atmospheric low-latitude state. It was defined as the number of days per year during which the atmospheric jet was located within a range of latitudes southward of the jet's climatological location. Both oceanic heat content and atmospheric regime occupation time series exhibit statistically significant spectral peaks in the bi-decadal range (not shown), and are essentially in quadrature. Such a definitive phase relationship between the oceanic and atmospheric variables is yet another proof for the coupled nature of the bi-decadal signal under consideration. Note that while the multi-year lags may characterize oceanic response to the atmospheric forcing anomalies due to ocean's large thermal and dynamical inertia (see the next paragraph),

the multi-year lag between an ocean variable and an atmospheric variable can only mean that there is a lag between this oceanic variable and the metric of the ocean–atmosphere heat flux that subsequently rearranges atmospheric circulation; this rearrangement is bound to happen quickly, on atmospheric intrinsic time scales.

Figure 5b shows the results from an ocean adjustment experiment, in which the ocean circulation responded to a permanent shift in the atmospheric forcing regime; the high-latitude and low-latitude regimes were computed by compositing the atmospheric time series over time intervals with positive and negative values of the projection onto the jet-shifting mode (Fig. 1b). The results in this figure are plotted in terms of a normalized Euclidean distance between the final and current zonally averaged SST states of the adjustment experiment; Euclidean distance between two vectors $\mathbf{x} \equiv \{x_i\}$ and $\mathbf{y} \equiv \{y_i\}$, $1 \leq i \leq N$, is given by $\{\sum_{i=1}^{N} (x_i - y_i)^2\}^{1/2}$.

Consider the oceanic adjustment from an initial low-latitude atmospheric-jet state to a final high-latitude state; the opposite case is analogous. The adjustment has two stages. During the fast advective stage (years 1–4 in Fig. 4b), the eastward jet relocates due to the northward shift of the line of zero wind-stress curl associated with the onset of the high-latitude regime. This stage is also characterized by the ocean jet's overshoot, so that its location at year 4 (not shown) is to the north of the ocean jet's final location; the latter coincides with the latitude of the atmospheric jet's high-latitude state. Associated with this circulation anomaly relative to the final, adjusted state, is a positive zonal SST anomaly north of the atmospheric jet's axis [see Fig. 9f of Kravtsov et al. (2006b)]. The overshoot of the ocean jet and the associated zonal SST anomaly are maintained, during years 5–15 (Fig. 4b), by the action

of oceanic baroclinic eddies, in exactly the same fashion as the climatological jet is maintained; see also Berloff (2005c) and Berloff et al. (2007).

The period of the coupled oscillation is related to the duration of the second, eddy-related stage of the adjustment. In particular, Kravtsov et al. (2006b, 2007a) have shown that the period of the oscillation depends on the ocean's bottom drag; in a coupled experiment with a strong bottom drag, the eddy-driven adjustment time scale was one half of that in the present experiment, and the period of the coupled oscillation was roughly 7–15 years. Furthermore, the coupled mode was not found in experiments employing a coarser-resolution, higher-viscosity ocean model, in which the eddy field was much weaker; accordingly, the coarse-resolution ocean adjustment did not have the eddy-driven stage at all [compare zonal SST curves in Figs. 9c,f of Kravtsov et al. (2006b)].

The SST anomalies associated with the eddy-driven adjustment influence the atmospheric state's PDF by increasing the probability of the low-latitude state for positive SST anomalies to the north of the high-latitude state's location, and by decreasing this probability for negative SST anomalies to the south of the low-latitude state's location. It is this coupled feedback that is responsible for the oscillatory behavior of the present model.

We model this effect of SST anomalies on the atmospheric statistics by the scalar, stochastic differential equation

$$dx = -V_x dt + \sigma dw; \tag{4}$$

here $x(t)$ is the temporal amplitude of the spatially coherent atmospheric jet-shifting mode, subscript x denotes a derivative with respect to x, and w is a

Wiener process whose increments have unit variance. The potential $V(x;y)$ depends parametrically on the "ocean state" y. It is convenient to think about y in terms of the position of the oceanic eastward jet, which affects the atmospheric potential through the associated SST anomalies: $y = +1$ thus corresponds to the oceanic jet's high-latitude state, and $y = -1$ to its low-latitude state. To compute V, we performed uncoupled integrations of the QG model's joint atmospheric and mixed-layer components forced by ocean circulations composited over the extreme phases of the coupled oscillation, denoted here by $y = \pm 1$; see Kravtsov et al. (2007a) for details. Each integration lasted 800 years and we denote by x the centered, normalized time series of the jet-axis position. The potentials $V(x;\ \pm 1)$ and standard deviations $\sigma(\pm 1)$ of the noise were determined by polynomial regression (Kravtsov et al. 2005b) assuming $V(x;\ \pm 1) = \sum_{i=0}^{I} a_i x^i$ and $I = 7$. The dependence of σ on oceanic state was weak (not shown), so we will later use state-independent noise in (4).

The resulting V profiles are plotted in Fig. 6a for the low-latitude ($y = -1$; light solid line) and high-latitude ($y = +1$; light dashed line) phases of the coupled oscillation. The potential in both cases consists of a pronounced dip at $x \approx 0.4$, which corresponds to the model's high-latitude state, and an additional flat "shoulder" centered at $x \approx -2$ for the low-latitude state. The ocean affects the atmospheric statistics by changing primarily the height of this low-latitude plateau of the potential V relative to its absolute, high-latitude state minimum; this results in roughly 10% changes in the probability of the atmospheric low-latitude jet state (Kravtsov et al. 2007a) over the course of the coupled oscillation.

3 Development of a mechanistic model

The coupled interdecadal oscillation described in section 2 is a highly nonlinear phenomenon. We develop in this section a conceptual model that combines the two essential ingredients of this variability: (i) the presence of low-latitude and high-latitude atmospheric states whose occupation is modulated by the ocean state; and (ii) an oceanic lagged response to atmospheric jet shifts between high- and low-latitude atmospheric regimes. Before we do so, we need to emphasize that the variability we describe is "coupled" in a somewhat different sense than "classical" coupled modes (for example, ENSO). Indeed, much of the atmospheric variability, including persistent states and transitions between them, is intrinsic. It forces the lagged oceanic response which, in turn, modulates the occurrences of atmospheric regimes and introduces some temporal regularity into these occurrences. Secondly, we do not attempt to model all of the QG model's variability by our mechanistic model, but only its "coupled" component. The full variability can be interpreted as a mixture of this coupled signal and white (red) noise in the atmosphere (ocean).

3.1 Atmospheric component and coupling

We assume that the atmospheric variable x, which represents the instantaneous position of the zonal jet, behaves according to Eq. (4), with $\sigma = 0.29$ day^{-1} and the potential $V(x;\, y)$ given by

$$V(x;\, y) = \frac{1}{500}\left(x + \frac{1}{2}\right)^4 - 0.1\left\{\exp\left[-\frac{1}{2}\left(x - \frac{1}{2}\right)^2\right] + a(y)\exp\left[-\frac{1}{2}\left(x+3\right)^2\right]\right\}. \quad (5)$$

Here y is the ocean-state (SST) variable, and

$$a(y) = \frac{1}{2}\left[(a_2 - a_1)y + (a_2 + a_1)\right], \tag{6}$$

where $a_1 \equiv a(-1) = 0.05$ and $a_2 \equiv a(1) = 0.6$. The potential $V(x;\, y)$ defined by Eqs. (5, 6) is shown in Fig. 6a for $a = a_2$ (heavy solid line) and $a = a_1$ (heavy dashed line). The heavy lines (solid and dashed), based on Eqs. (5, 6), bracket the light lines (solid and dashed, respectively) determined by the polynomial fit to the QG model's potential $V(x;\, \pm 1)$ (cf. Kravtsov et al. 2006b, 2007a); the two fits, for $y = \pm 1$, agree with the qualitative dependence of the potential on the ocean-state parameter $a(y)$: when the ocean is in its high-latitude state ($y = 1$) the height of the atmospheric low-latitude state's plateau decreases relative to its position subject to the ocean's low-latitude state ($y = -1$).

As we mentioned above, the variation between the conditional potentials given by Eqs. (5,6) are larger in magnitude compared to the values derived from the QG model simulation. This discrepancy accounts for the fact that QG–model-based estimates involve substantial averaging, due to the compositing, and thus underestimate the range of the potential's actual realizations. In order to check if this explanation is sensible, we have applied the fitting procedure used to define the conditional QG model's potential functions to the output of our conceptual coupled model (see sections 3.3 and 4), whose oceanic variable was contaminated by the red noise to represent the processes not explicitly resolved by this model. The results are presented in Fig. 6b and show that the compositing procedure may indeed be responsible for the underestimation of actual difference between the potential functions representing high-latitude and low-latitude states.

The behavior of the conceptual atmospheric model (4–6) is summarized in Fig. 7 in terms of its PDF (Fig. 7a) and power spectra (Fig. 7b) for two values of y: $y = 1$ (ocean's high-latitude state; solid lines) and $y = -1$ (ocean's low-latitude state; dashed lines). In both cases, the PDF is strongly skewed, as expected from the shape of the potential V (Fig. 6), thus defining two quasi-stationary states; mixture modeling (Smyth et al. 1999) based on the jet position's time series confirms the assertion of two distinct, statistically significant Gaussian components (not shown). Both spectra have a red-noise character and roll off to a white spectrum for frequencies $f < 1\,\mathrm{year}^{-1}$. For $y = 1$ (solid lines), the probability of the atmospheric low-latitude state, as well as the spectral power at low frequencies, increases relative to these quantities for $y = -1$ (dashed lines).

3.2 Ocean component

Evolution of the oceanic variable y is governed by

$$\dot{y} = -\lambda y + Ax(t - T_\mathrm{d}), \tag{7}$$

where the dot denotes the derivative with respect to time. The ocean responds to the atmospheric forcing x after a delay $T_\mathrm{d} = 5$ years, and is characterized by the linear decay time scale of $\lambda^{-1} = 2$ years. The fact that our conceptual ocean "sees" the exact atmospheric history delayed by 5 years is somewhat artificial, especially given a relatively flat spectrum of atmospheric variability shown in Figs. 4a and 7b. This choice was dictated by our intention to analyze the conceptual coupled model analytically (see section 4). An alternative would be to use a smoothed version of the atmospheric history to force the

ocean model. We note, however, that the presence of linear damping with a multi-year time scale effectively plays the role of such a smoother. Therefore, we do not expect qualitative differences between the models with instantaneous and smooth atmospheric forcing and choose a simpler model (7).

The ocean adjustment to a permanent switch of the atmospheric forcing regime, from the high-latitude to the low-latitude state or vice versa, mimics the sum of the two adjustment times shown in Fig. 4b; this sum is dominated by the slow, eddy-driven stage of the QG model's adjustment (Fig. 4b). The delay thus reflects the property of the oceanic jet to stay at position $y = +1/-1$ (oceanic high-/low-latitude state) for several years without immediately responding to the switch of the atmospheric forcing to $x = -1/+1$ (atmospheric low-/high-latitude state) and, at the same time, maintaining SST patterns supportive of the atmospheric jet position at $x = -1/+1$. Kravtsov et al. (2006b) show, by considering two-dimensional patterns of SST anomalies during such an adjustment (their Figs. 6 and 9) and estimating the effect of the latter anomalies on the atmospheric jet's PDF, that the effective delay time in the coupled system is somewhat shorter than that suggested by the simple, zonally averaged SST metric used in Fig. 5b. This argument explains our choice of the delay time in (7) to be only 5 yr, rather than the 10 yr suggested by Fig. 5.

On the other hand, the parameter λ describes frictional processes which are only able to damp oceanic anomalies, rather than maintain them. The scaling factor $A^{-1} = 140$ days was chosen so that the standard deviation of y is equal to unity; y thus represents, formally, a normalized time series of the QG model's leading oceanic EOF, which captures the shifting of the jet.

3.3 Coupled model's variability

The conceptual coupled model governed by Eqs. (4–7), was integrated for 4000 years with a time step of $\Delta t = 1$ day. The Fourier spectrum of the resulting daily data is shown in Fig. 8. The atmospheric spectrum has a general red-noise shape, as in Fig. 7b, but exhibits a broad spectral peak with a central frequency that corresponds to the period of $T \approx 15$ years, as well as secondary peaks at higher frequencies. The ocean spectrum has a much higher slope; it exhibits the same spectral peaks as the atmospheric spectrum and rolls off to a white spectrum at frequencies $f < 1/30$ year^{-1}. This behavior will be explained in section 4 by developing a counterpart of the conceptual coupled model (4)–(7) that is solvable nearly analytically.

4 Theoretical analysis

4.1 Atmospheric low-frequency variability as a random telegraph process

The equation (4), for a fixed y, describes the motion of a particle in the potential $V(x)$ given by Eqs. (5,6) (Bhattacharya et al. 1982; Gardiner 1985; Bryan and Hansen 1993; Stommel and Young 1993; Cessi 1994; Miller et al. 1994). The PDF $\phi(x)$ evolves according to the corresponding Fokker–Planck equation

$$\partial_t \phi = \partial_x (V_x \phi) + \kappa \partial_x^2 \phi, \tag{8}$$

where the symbols ∂_t and ∂_x denote the partial t- and x-derivatives, respectively, while the diffusion coefficient κ is given by

$$\kappa = \sigma^2 \Delta t/2. \tag{9}$$

The stationary solution to Eq. (9) is

$$\phi_s(x) = C \exp(-V(x)\kappa^{-1}), \tag{10}$$

where the constant C is chosen so that $\int_{-\infty}^{\infty} \phi_s(x)\, dx = 1$. The stationary PDFs (not shown) given by Eq. (10), with V defined by Eqs. (5, 6) for $y = \pm 1$, closely resemble those from direct numerical simulation (Fig. 7a).

In the case of two potential wells centered at $x = x_{\rm L}$ and $x = x_{\rm H}$, and separated by a potential barrier at $x = x_0$ ($x_{\rm L} < x_0 < x_{\rm H}$), one can derive analytical approximations for the mean escape times of a particle from one well to the other (Gardiner 1985; Ghil and Childress 1987) in the limit of weak diffusion $\kappa \ll \min(\Delta V_{\rm L}, \Delta V_{\rm H})$, where $\Delta V_{\rm L} \equiv V(x_0) - V(x_{\rm L})$ or $\Delta V_{\rm H} \equiv V(x_0) - V(x_{\rm H})$ is the depth of the corresponding well. The resulting estimates of the mean escape times $< t >$ depend exponentially on $\kappa^{-1}\Delta V$:

$$\begin{aligned} &< t_{\rm L\to H} > \sim \exp(\kappa^{-1}\Delta V_{\rm L}), \\ &< t_{\rm H\to L} > \sim \exp(\kappa^{-1}\Delta V_{\rm H}). \end{aligned} \tag{11}$$

Kramers (1940) has shown that the low-frequency behavior of the probabilities $P_{x_{\rm L}} \equiv \int_{-\infty}^{x_0} \phi(x,\, t)\, dx$ and $P_{x_{\rm H}} \equiv \int_{x_0}^{-\infty} \phi(x,\, t)\, dx$ of a particle to be in one or the other potential well are governed by the equation for a random telegraph process (Appendix A), in which only two states $x_{\rm L}$ and $x_{\rm H}$ are allowed and the decay rates $\mu_{\rm L}$ and $\mu_{\rm H}$ toward the minima of the potential wells are inversely

proportional to the corresponding mean escape times. The mean M_{RT}, autocorrelation C_{RT}, and Fourier spectrum S_{RT} of a random telegraph process are given in Appendix A.

The high-frequency behavior associated with fluctuations around either of the two equilibrium states x_{L} or x_{H} can be approximated by an Ornstein–Uhlenbeck process (Wax 1954; Bryan and Hansen 1993; Cessi 1994); the corresponding spectra $S_{x_{\mathrm{L}}}$ and $S_{x_{\mathrm{H}}}$ are

$$\begin{aligned} S_{x_{\mathrm{L}}} &= \frac{\sigma^2 dt}{\omega^2 + V_{xx}(x_{\mathrm{L}})^2}, \\ S_{x_{\mathrm{H}}} &= \frac{\sigma^2 dt}{\omega^2 + V_{xx}(x_{\mathrm{H}})^2}. \end{aligned} \tag{12}$$

The full atmospheric spectrum S_{a} can be obtained by patching the above approximations for low and high frequencies (Cessi 1994), and is given by

$$S_{\mathrm{a}} = S_{\mathrm{RT}} + \frac{\mu_{\mathrm{H}} S_{x_{\mathrm{L}}} + \mu_{\mathrm{L}} S_{x_{\mathrm{H}}}}{\mu_{\mathrm{L}} + \mu_{\mathrm{H}}}. \tag{13}$$

The analytical approximations used above to estimate the spectra of the solution to a double-well potential problem rely on the assumptions that do not hold in our case of interest, where the potential consists of one major well and an additional plateau (Fig. 6). It turns out, however, that these spectra are still well described by the fit (13), in which $x_{\mathrm{L}} = -2.25$ and $x_{\mathrm{H}} = 0.43$. The quantities μ_{L} and μ_{H} were estimated directly from the simulated data sets' residence-time information; for $y = -1$, $\mu_{\mathrm{L},-1} \approx 0.02$ and $\mu_{\mathrm{H},-1} \approx 0.005$, while for $y = +1$, $\mu_{\mathrm{L},+1} \approx 0.03$ and $\mu_{\mathrm{H},+1} \approx 0.004$. In both cases, it turns out that using the value of $\omega_0 = V_{xx}(x_{\mathrm{L}}) = V_{xx}(x_{\mathrm{H}}) = 0.15$ day^{-1} in the high-frequency spectra (12) does provide a fairly good fit to this portion of the spectrum, despite the assumption of $V_{xx}(x_{\mathrm{L}}) = V_{xx}(x_{\mathrm{H}})$ being clearly a pretty crude one.

The resulting sum of high- and low-frequency spectra (Fig. 7b, heavy lines; Eq. 13) matches the spectra obtained from a direct model simulation very well.

The time-mean values of x in the two uncoupled, atmosphere-only simulations for $y = \pm 1$ can be found from Eq. (A.6); they also match the values estimated directly from the model simulations and are equal to $< x >_{\pm 1} = \bar{x}_{\pm 1} \approx \pm 0.1$.

4.2 A simplified conceptual model

In order to further simplify the conceptual coupled system (4)–(7), we assume that the sole effect of the oceanic variability on the atmospheric statistics is to change, on a slow time scale, the expected value $\bar{x}(y)$ of x, while neglecting the dependencies of $\mu_{\rm L}$ and $\mu_{\rm H}$ on y (see the preceding subsection). Thus,

$$\begin{aligned} x &= \bar{x}(y) + x', \\ \bar{x}\,(y) &= -Dy, \end{aligned} \tag{14}$$

where $D = 0.1$ and x' is a stationary process whose spectrum is approximated by $0.5(S_{\rm a,+1} + S_{\rm a,-1})$; see Eq. (13). Using Eq. (14) to rewrite Eq. (7) yields

$$\dot{y} = -\lambda y - ADy(t - T_{\rm d}) + Ax'. \tag{15}$$

The latter is formally identical to a classical delayed oscillator equation (Bhattacharya et al. 1982; Suarez and Schopf 1988; Battisti and Hirst 1989; Bar-Eli and Field 1998; Marshall et al. 2000), except that x' is a red-noise, rather than a white-noise process. More importantly, however, the possibility of active coupling between x and y stems from the atmospheric model's nonlinear sensitivity to the oceanic state; the latter sensitivity is expressed via non-Gaussian

changes to the atmospheric-flow PDF, namely the atmospheric mean state changes as in (14); see also Neelin and Weng (1999). The "delayed-feedback" term and the "stochastic-forcing" term in (15) are thus multiplied by the same factor A to explicitly reflect this property.

4.3 Analytical model results

4.3.1 Spectrum and covariance

Assuming, in Eq. (15), $y = \hat{y}e^{i\omega t}$ and $x' = \hat{x}'e^{i\omega t}$, where $i^2 = -1$, one obtains for the oceanic spectrum $S_{\rm o} =< \hat{y}\hat{y}^* >$ the expression

$$S_{\rm o}(\omega) = \frac{0.5A^2[S_{\rm a,+1} + S_{\rm a,-1}]}{[AD\cos(\omega T_{\rm d}) + \lambda]^2 + [\omega - AD\sin(\omega T_{\rm d})]^2}. \tag{16}$$

The atmospheric spectrum $S_{\rm a,\,c}$ of the coupled simulation can be found, using Eq. (14), to be

$$S_{\rm a,\,c}(\omega) = 0.5[S_{\rm a,+1} + S_{\rm a,-1}] + \frac{D}{A}S_{\rm o}(\omega)[\omega\sin(\omega T_{\rm d}) - \lambda\cos(\omega T_{\rm d})], \tag{17}$$

where the first member of the sum represents the uncoupled spectrum $< \hat{x}'\hat{x}'^* >$, while the second term is due to coupling. The resulting analytical spectra are plotted as heavy solid lines in Fig. 8 and match remarkably well those obtained directly from the simulation of the conceptual coupled model (4)–(7). The discrepancies at very low frequencies are due, most likely, to the neglect of the $\mu_{\rm L}$- and $\mu_{\rm H}$-dependencies on the oceanic state y (see the preceding subsection). The otherwise excellent agreement between the full conceptual model simulation and its simplified analytical counterpart (15) justifies the latter approximation.

The most obvious effect of coupling on the model spectra is to decrease the power at very low frequencies, which can immediately be seen from the expressions (16, 17) estimated at $\omega = 0$, because both $S_{\mathrm{o}}(0)$ and $S_{\mathrm{a,\,c}}(0)$ decrease as the coupling coefficient D increases. This damping arises because of the oceanic control of the atmospheric variability; at low frequencies $\omega \ll T_{\mathrm{d}}^{-1}$, positive y anomalies induce a decay in x anomalies [see Eq. (14)] and vice versa.

More interestingly, coupling can also produce spectral peaks. To obtain the locations ω_{m} of these spectral peaks, we differentiate $S_{\mathrm{o}}(\omega)$ in (16) with respect to ω and set the result to zero. Let us introduce nondimensional quantities $\omega^{\dagger} \equiv \omega_{\mathrm{m}} T_{\mathrm{d}}$, $\omega_{\mathrm{a}}^{\dagger} \equiv (\mu_{\mathrm{L}} + \mu_{\mathrm{H}}) T_{\mathrm{d}}$, $\lambda^{\dagger} \equiv \lambda T_{\mathrm{d}}$, and $A^{\dagger} \equiv A D T_{\mathrm{d}}$; then the resulting approximate equation for $\omega_{\mathrm{m}} \ll \omega_0$ is

$$\frac{\omega^{\dagger}}{A^{\dagger}} \left\{ 1 + \frac{2[(A^{\dagger} \cos\omega^{\dagger} + \lambda^{\dagger})^2 + (\omega^{\dagger} - A^{\dagger} \sin\omega^{\dagger})^2]}{\omega_{\mathrm{a}}^{\dagger 2} + \omega^{\dagger 2}} \right\} = (\lambda^{\dagger} + 1) \sin\omega^{\dagger} + \omega^{\dagger} \cos\omega^{\dagger}. \quad (18)$$

The spectral maxima are those solutions of Eq. (18) for which the second derivative is negative $S_{\mathrm{o}\,\omega\omega} < 0$. The dependence of spectral peaks on model parameters is complex and will be further discussed in the next subsection. For the set of control parameters used thus far, the lowest-frequency solution of Eq. (18) is $\omega^{\dagger} \approx 2$, which corresponds to a dimensional period of $T \equiv 2\pi T_{\mathrm{d}}/\omega^{\dagger} \approx \pi T_{\mathrm{d}} = 15$ years (see Fig. 8).

The lagged covariances of the conceptual coupled model solution $C_{\mathrm{o}}(\tau)$ and $C_{\mathrm{a,\,c}}(\tau)$ are given by

$$C_{\mathrm{o}}(\tau) = \frac{1}{2\pi} \int_{-\infty}^{\infty} S_{\mathrm{o}}(\omega) e^{i\omega\tau}\, d\omega,$$

$$C_{\mathrm{a,\,c}}(\tau) = \frac{1}{2\pi} \int_{-\infty}^{\infty} S_{\mathrm{a,\,c}}(\omega) e^{i\omega\tau}\, d\omega, \tag{19}$$

respectively, and are estimated in appendix B. These analytical estimates match very well the direct estimates of covariances based on the full conceptual model simulation (Eqs. 4–7); both analytical and direct estimates are shown in Fig. 9. The oceanic lagged covariance (Fig. 9a) is characterized by a gradual decay from $C_{\mathrm{o}}(0) = 1$ to minima at $\tau^* \approx \pm T/2$, at which the autocorrelation has a relatively large magnitude of $C_{\mathrm{o}}(\tau^*) \approx -0.2$ (compare this with reverse of the sign of circulation anomalies in Figs. 3a,c,e). In contrast, the atmospheric autocorrelation is very small for all $|\tau| > 1$ year; nevertheless, the sharp drop of $C_{\mathrm{a,\,c}}$ that occurs at $\tau^{**} \approx T_{\mathrm{d}}$ and a subsequent slow decay of correlation at $|\tau| > \tau^{**}$ are both the effects of coupling.

In order to put these results into a perspective, we also plot, in Fig. 10, the autocorrelation functions of the coupled QG model's ocean kinetic energy and atmospheric jet position time series. Both autocorrelations were computed for the annual data, unlike the daily data used in Fig. 9 for the conceptual model's quantities. The oceanic autocorrelation in Fig. 10a decays somewhat faster than its conceptual model's counterpart (Fig. 9a) at small lags up to ± 3 yrs, and the dips in autocorrelation at ± 7 yr are less pronounced. This reflects the presence, in the QG model's time series, of the variability not directly associated with the coupled dynamics of the conceptual model. We fitted the QG model's oceanic autocorrelation function much better by mixing the conceptual model's time series with the red-noise process characterized by the autocorrelation of 0.99 at a lag of one day, and the same annual variance as in the original conceptual model time series (not shown). This contaminated signal was used to produce Fig. 6b.

Finally, the qualitative structure of the QG model's atmospheric jet position autocorrelation (Fig. 10b) is consistent with that in Fig. 9b; it quickly drops to essentially zero and maintains zero values within the first few years, then exhibits a second drop to negative values at the lag of ± 7 years and a subsequent few-year-long come back to slightly positive values. We conclude that our conceptual model captures essential features of the coupled variability simulated by the full QG model.

4.3.2 Parameter sensitivity

We explore sensitivity of the decadal-to-interdecadal variability in model (15) to the coupling coefficient D and the ocean's linear decay parameter λ, by changing each in turn, while keeping the other fixed at its control value. Figure 11 shows analytical spectra as functions of D. If the coupling is weak ($D = 0.01$; Fig. 11a), both oceanic and atmospheric spectra do not differ significantly from the uncoupled case $D = 0$, which is characterized by a white atmospheric spectrum and red-noise oceanic behavior. For an intermediate coupling strength ($D = 0.05$; Fig. 11b), an interdecadal peak that is still broad and weak arises. The amplitude of this interdecadal oscillation increases, while the period and the bandwidth of the associated spectral peak decrease as the coupling strength increases further to normal ($D = 0.1$; Fig. 11c) and high ($D = 0.15$; Fig. 11d) values.

The dependence of the coupled oscillation on λ is shown in Fig. 12. Panels (a)–(d) present results for progressively larger values of λ. In addition to straightforward damping of the ocean variance at all frequencies and "diffusing" the spectral peak, increasing λ decreases the oscillation period.

5 Concluding remarks

5.1 Summary

We have constructed a conceptual model of mid-latitude climate variability that incorporates two essential aspects of the novel, highly nonlinear decadal mode found recently in a coupled quasi-geostrophic (QG) model by Kravtsov et al. (2006b, 2007a), namely: (i) nonlinear sensitivity of the atmospheric circulation to SST anomalies; and (ii) extended, mainly eddy-driven adjustment of the ocean's wind-driven gyres to the corresponding changes in the atmospheric forcing regime.

The dynamics of the QG model's coupled decadal mode was summarized in section 2. Atmospheric intrinsic variability is characterized by irregular shifts of the model's jet stream between two anomalously persistent states, located north and south of its time-mean position (Fig. 1). The oceanic response is dominated by changes in the position and intensity of its eastward jet; the latter is largely maintained by high-frequency eddy interactions (Fig. 2). These interactions also maintain ocean circulation anomalies in the course of the coupled oscillation (Figs. 3, 4, 5a), which has a period of about 20 years. The period is related to the lag associated with the ocean's adjustment to atmospheric forcing transitions between its high-latitude and low-latitude regimes (Fig. 5b). The portion of this lag during which the ocean eddies create circulation anomalies and ensuing SST anomalies that are supportive of the opposite atmospheric-jet state determines the effective lag at work in the coupled system; this lag is thus shorter than that apparent in Fig. 5b.

The jet-shifting mode that dominates atmospheric intrinsic variability was modeled by Eq. (4), which describes the motion of a particle in a non-convex potential. Such a potential was obtained by fitting the jet position of the full, coupled QG model, and is characterized by a deep "high-latitude" well and a low-latitude "plateau" (Fig. 6). Eddy-driven SST anomalies affect the height of this plateau relative to the potential's high-latitude minimum.

A conceptual model was developed in section 3 to describe the key aspects of the coupled QG model's behavior. The conceptual model has two variables, one of which represents the jet-shifting mode x, whose evolution is governed by Eq. (4), while the other is the oceanic variable y, representing the position of the oceanic eastward jet; this position is associated, in the QG model, with SST anomalies that can change the shape of the atmospheric potential V. The potential $V(x;\ y)$ is given by Eqs. (5, 6) and depends linearly on y in a way consistent with the QG-model-based fit. The atmospheric model's strongly non-Gaussian PDF (Fig. 7a) and spectra (Fig. 7b) thus depend on the "ocean" state. The SST equation (7) has a linear damping component and directly responds to atmospheric forcing x with a lag of a few years; the latter delay mimics the QG model's adjustment. The coupled model (4)–(7) supports an interdecadal oscillation (Fig. 8) similar to that in the QG model (Fig. 4a; also compare Figs. 9 and 10).

In section 4, we have further simplified the conceptual model by representing its atmospheric component as a sum of a random telegraph process (see Appendix A) at low frequencies and an Ornstein–Uhlenbeck process at high frequencies (Cessi 1994). Both the expectation value $<x>$ and the spectrum of x depend on the ocean variable y and are in excellent agreement with direct simulations (Fig. 7b). Neglecting the latter spectral dependence results

in a simplified model (14, 15), which has the form of a classical delayed oscillator and explains remarkably well the simulated spectra (Fig. 8) and time-correlation function (Fig. 9; see Appendix B for the analytical derivation).

The analytical model (14, 15) is then used to study the dependence of the coupled oscillation on the coupling coefficient (Fig. 11) and oceanic damping (Fig. 12). Most importantly, the value of the coupling coefficient reflects the ability of SST anomalies to affect the atmospheric long-term mean; hence, no oscillatory coupled mode exists in a unimodal atmospheric setting.

5.2 Discussion

The present conceptual model (4)–(7), in its simplified form (14, 15), is formally similar to delayed oscillators formulated elsewhere (Marshall et al. 2000; Dewar 2001); the dynamics it represents, though, is fundamentally different. Most importantly, the oscillation is entirely based upon coupling; it does not exist if the ocean is not allowed to affect the atmosphere. In contrast, the linear models summarized by Marshall et al. (2000) can exhibit spectral peaks in an uncoupled setting, in which ocean-state-independent atmospheric noise excites a damped oceanic standing-wave oscillation. Coupling merely enhances such spectral peaks, since a delayed feedback due to planetary wave propagation tends to overcome damping.

Extending the linear-model analysis of Marshall et al. (2000), Dewar (2001) studied effects of oceanic turbulence on coupled mid-latitude variability. The primary effect of coupling in Dewar (2001) was to arrest the inter-gyre heat flux due to the ocean's intrinsic variability on decadal and longer time scales; the

atmospheric decadal variability was thus completely controled by the oceanic processes. In our model, as in Marshall et al. (2000), the atmospheric intrinsic variability is essential in launching the adjustment process; our oceanic eddy-driven adjustment is, however, entirely different from the planetary-wave or purely advective adjustment (Jin 1997; Saravanan and McWilliams 1998; Neelin and Weng 1999; Czaja and Marshall 2001; Marshall et al. 2000). Differences are evident in both spatial pattern and time dependence (Dewar 2003; Kravtsov et al. 2006b, 2007a).

Our conceptual model emphasizes nonlinearity of the atmospheric intrinsic variability as an essential ingredient of coupling. In particular, the eddy-driven SST anomalies change the statistics of the atmospheric high-latitude and low-latitude regimes, thereby affecting the conditional expectation of the atmospheric jet position; Neelin and Weng (1999) called this a "deterministic feedback." The sign and magnitude of this SST feedback are like those in other conceptual models. In contrast, though, to the *ad hoc* formulation of the feedback by the latter authors, ours is based on the dynamics of a fairly realistic atmospheric model (Kravtsov et al. 2005a).

The issue of nonlinear atmospheric sensitivity is intimately related to the concept of atmospheric flow regimes — a few anomalously persistent flow patterns, whose occurrence frequency depends on oceanic state. The existence of such a nongaussian behavior in the observational data sets is still a subject of an ongoing debate (Hsu and Zwiers 2001; Stephenson et al. 2004; Deloncle et al. 2007). Berner and Branstator (2007) identified significant deviations from gaussianity in a four-dimensional phase space of an atmospheric general circulation model and showed that the corresponding phase-space structure can be described in terms of two off-centered Gaussian distributions. This is

consistent with the behavior of our atmospheric QG model in the sense that the latter does not produce bimodal probability density function, but is still characterized by two distinctive atmospheric states.

Finally, our coupled QG model is by itself but a metaphor for climate variability. The simplifications within this model that may strongly affect the simulated climate behavior include, among other things, extreme vertical truncation and cartesian geometry. We should also mention that the thermal coupling in our QG model assumes that ocean-induced SST anomalies affect the atmospheric interior circulation directly, whereas in reality the air–sea interaction involves complex chain of physical processes and feedbacks associated with atmospheric boundary-layer dynamics. This may potentially exaggerate the atmospheric response to oceanic variability. The above issues need to be addressed by experimenting with progressively more complex coupled climate models.

To conclude, the coupled mechanism summarized in this paper with the help of a conceptual climate model calls for GCM studies of mid-latitude coupling that will explore more highly nonlinear atmospheric regimes, as well as eddy-resolving ocean components.

Acknowledgements. We are grateful to two anonymous reviewers for their thoughtful comments which helped improve the presentation. This research was supported by National Science Foundation grant OCE-02-221066 (all co-authors) and the Department of Energy grant DE-FG-03-01ER63260 (MG and SK).

A Random telegraph process

A random telegraph signal $x(t)$ can only attain one of the two values $x_{\rm L}$ or $x_{\rm H}$. Given the value of $x = x(t_0)$ at initial time $t = t_0$, the conditional probabilities $P(x_{\rm L},\, t|x,\, t_0)$ and $P(x_{\rm H},\, t|x,\, t_0)$ of $x(t) = x_{\rm L}$ and $x(t) = x_{\rm H}$ at some time $t > t_0$, respectively, are goverened by the following master equation (Gardiner 1985):

$$\begin{aligned} \dot{P}(x_{\rm L},\, t|x,\, t_0) &= -\mu_{\rm L} P(x_{\rm L},\, t|x,\, t_0) + \mu_{\rm H} P(x_{\rm H},\, t|x,\, t_0), \\ \dot{P}(x_{\rm H},\, t|x,\, t_0) &= -\mu_{\rm H} P(x_{\rm H},\, t|x,\, t_0) + \mu_{\rm L} P(x_{\rm L},\, t|x,\, t_0), \end{aligned} \tag{A.1}$$

in which the dot denotes the derivative with respect to time and

$$P(x_{\rm L},\, t|x,\, t_0) + P(x_{\rm H},\, t|x,\, t_0) = 1. \tag{A.2}$$

The initial condition for Eq. (A.1) can be written as

$$P(x',\, t_0|x,\, t_0) = \delta_{x,\, x'}, \tag{A.3}$$

where $\delta_{x,\, x'}$ is the Kronecker delta.

The solution of Eq. (A.1) subject to conditions (A.2, A.3) is

$$\begin{aligned} P(x_{\rm L},\, t|x,\, t_0) &= \frac{\omega_{\rm H}}{\omega_{\rm L} + \omega_{\rm H}} + \left(\frac{\omega_{\rm L}}{\omega_{\rm L} + \omega_{\rm H}} \delta_{x_{\rm L},\, x} - \frac{\omega_{\rm H}}{\omega_{\rm L} + \omega_{\rm H}} \delta_{x_{\rm H},\, x} \right) \exp[-(\omega_{\rm L} + \omega_{\rm H})(t - t_0)], \\ P(x_{\rm H},\, t|x,\, t_0) &= \frac{\omega_{\rm L}}{\omega_{\rm L} + \omega_{\rm H}} - \left(\frac{\omega_{\rm L}}{\omega_{\rm L} + \omega_{\rm H}} \delta_{x_{\rm L},\, x} - \frac{\omega_{\rm H}}{\omega_{\rm L} + \omega_{\rm H}} \delta_{x_{\rm H},\, x} \right) \exp[-(\omega_{\rm L} + \omega_{\rm H})(t - t_0)]. \end{aligned} \tag{A.4}$$

The stationary probabilities $P_{\rm s}(x_{\rm L})$ and $P_{\rm s}(x_{\rm H})$ can be found from Eq. (A.4) by letting $t_0 \to -\infty$:

$$P_{\rm s}(x_{\rm L}) = \frac{\mu_{\rm H}}{\mu_{\rm L} + \mu_{\rm H}},$$

$$P_{\rm s}(x_{\rm H}) = \frac{\mu_{\rm L}}{\mu_{\rm L} + \mu_{\rm H}}. \tag{A.5}$$

The stationary mean $M_{\rm RT} \equiv < x >_{\rm s} \equiv x_{\rm L} P_{\rm s}(x_{\rm L}) + x_{\rm H} P_{\rm s}(x_{\rm H})$, where the angle brackets denote ensemble average, is given therewith by

$$M_{\rm RT} = \frac{\mu_{\rm H} x_{\rm L} + \mu_{\rm L} x_{\rm H}}{\mu_{\rm L} + \mu_{\rm H}}. \tag{A.6}$$

The stationary time correlation function $< x(t)x(s) >_{\rm s} \equiv \sum_{xx'} P(x,\, t|x',\, s) P_{\rm s}(x')$ is also easily computed from (A.4, A.5):

$$< x(t)x(s) >_{\rm s} = < x >_{\rm s}^2 + \frac{\mu_{\rm L}\mu_{\rm H}}{(\mu_{\rm L} + \mu_{\rm H})^2} (x_{\rm H} - x_{\rm L})^2 \exp[-(\mu_{\rm L} + \mu_{\rm H})|\tau|]; \tag{A.7}$$

it is only a function of $\tau = t - s$, because of the translational invariance of the defining process (A.1). Thus, the autocorrelation $C_{\rm RT}(\tau) \equiv < x(t)x(s) >_{\rm s} - < x >_{\rm s}^2$ is

$$C_{\rm RT}(\tau) = \frac{\mu_{\rm L}\mu_{\rm H}}{(\mu_{\rm L} + \mu_{\rm H})^2} (x_{\rm H} - x_{\rm L})^2 \exp[-(\mu_{\rm L} + \mu_{\rm H})|\tau|]. \tag{A.8}$$

The spectrum of x, $S_{\rm RT}(\omega)$, is the Fourier transform of the autocorrelation function (A.8):

$$S_{\rm RT}(\omega) = \int_{-\infty}^{\infty} C_{\rm RT}(\tau) e^{-i\omega\tau}\, d\tau, \tag{A.9}$$

where $i^2 = -1$. The approximate expression for $S_{\rm RT}(\omega)$ has been given by Kramers (1940) and Gardiner (1985):

$$S_{\rm RT}(\omega) = \frac{2\mu_{\rm L}\mu_{\rm H}(x_{\rm H} - x_{\rm L})^2}{(\mu_{\rm L} + \mu_{\rm H})[(\mu_{\rm L} + \mu_{\rm H})^2 + \omega^2]}. \tag{A.10}$$

B Covariance of analytical coupled solution

Let us define, as in section 4c, dimensionless quantities $(\omega^\dagger,\ \omega_{\rm L}^\dagger,\ \omega_{\rm H}^\dagger,\ \omega_0^\dagger,\ \lambda^\dagger,\ \sigma^\dagger,\ A_0^\dagger) \equiv (\omega,\ \mu_{\rm L},\ \mu_{\rm H},\ \omega_0,\ \lambda,\ \sigma,\ A)T_{\rm d}$, $\omega_{\rm a}^\dagger \equiv \omega_{\rm L}^\dagger + \omega_{\rm H}^\dagger$, and $A^\dagger \equiv DA_0^\dagger$; the dimensionless oceanic spectrum $\tilde{S}_{\rm o} \equiv S_{\rm o}/T_{\rm d}$, where $S_{\rm o}$ is given by Eq. (16), is

$$\tilde{S}_{\rm o}(\omega^\dagger) = \frac{A_0^{\dagger 2}}{(A^\dagger \cos\omega^\dagger + \lambda^\dagger)^2 + (\omega^\dagger - A^\dagger \sin\omega^\dagger)^2} \left\{ \frac{2(\omega_{\rm L}^\dagger \omega_{\rm H}^\dagger/\omega_{\rm a}^\dagger)(x_{\rm H} - x_{\rm L})^2}{\omega_{\rm a}'^2 + \omega^{\dagger 2}} + \frac{2\sigma^{\dagger 2}(\Delta t/T_{\rm d})}{\omega_0^{\dagger 2} + \omega^{\dagger 2}} \right\}, \quad \text{(B.1)}$$

while the expression (19) for ocean covariance can be rewritten as

$$C_{\rm o}(\tau^\dagger) = \frac{1}{2\pi} \int_{-\infty}^{\infty} \tilde{S}_{\rm o}(\omega^\dagger) e^{i\omega^\dagger \tau^\dagger}\ d\omega^\dagger, \quad \text{(B.2)}$$

where $\tau^\dagger \equiv \tau/T_{\rm d}$.

The integral (B.2) can be estimated by standard methods (Churchill 1960) via integrating the complex function $F(z) \equiv \tilde{S}_{\rm o}(z) e^{iz\tau^\dagger}$, with $z \equiv \xi + i\eta$, counterclockwise along the real axis and around the boundary of the upper half of the circle $|z| = R$ for $\tau^\dagger > 0$, or lower half of this circle otherwise, and taking the limit of $R \to \infty$. The integrand is analytic within the integration contour except for a countable set of simple poles, and uniformly converges to zero as $R \to \infty$. Call K_n the residue of F at the n-th pole; then the integral (B.2) is given by

$$C_{\rm o}(\tau^\dagger) = i \sum_n K_n. \quad \text{(B.3)}$$

One can show that contributions to the integral (B.2) due to the poles $z = i\omega_{\rm a}^\dagger$ and $z = i\omega_0^\dagger$ are negligible. It is convenient, therefore, to rewrite $F(z)$ as

$$F(z) = f(z)/g(z), \quad \text{(B.4)}$$

where

$$f(z) = A_0^{\dagger 2} e^{iz\tau^\dagger} \left\{ \frac{2(\omega_{\rm L}^\dagger \omega_{\rm H}^\dagger / \omega_{\rm a}^\dagger)(x_{\rm H} - x_{\rm L})^2}{\omega_{\rm a}^{\dagger 2} + z^2} + \frac{2\sigma^{\dagger 2}(dt/T_{\rm d})}{\omega_0^{\dagger 2} + z^2} \right\} \tag{B.5}$$

and

$$g(z) = (A^\dagger \cos z + \lambda^\dagger)^2 + (z - A^\dagger \sin z)^2. \tag{B.6}$$

The poles $g(z) = 0$ that have positive imaginary parts are given by

$$\begin{aligned} A^\dagger \cos\xi &= (\eta - \lambda^\dagger) e^{-\eta}, \\ A^\dagger \sin\xi &= \xi e^{-\eta}, \end{aligned} \tag{B.7}$$

which, for the control set of model parameters, has approximate solutions $z_{n,\pm} \equiv \xi_{n,\pm} + i\eta_{n,\pm}$

$$\begin{aligned} &\xi_{0,\pm} \approx \pm 2.23, \quad \eta_{0,+} = \eta_{0,-} = \eta_0 \approx 0.772, \\ &\xi_{n,\pm} \approx \pm\left(\frac{\pi}{2} + 2\pi n\right), \quad \eta_{n,+} = \eta_{n,-} = \eta_n \approx \ln\frac{\xi_{n,+}}{A^\dagger}; \quad n \geq 1. \end{aligned} \tag{B.8}$$

The residues associated with these poles can be grouped as

$$K_n = \frac{f(z_{n,+})}{g'(z_{n,+})} + \frac{f(z_{n,-})}{g'(z_{n,-})}; \tag{B.9}$$

it can easily be shown that all of K_n have zero real parts, so the integral (B.3) is a real function of $\tau^\dagger$.

The covariance is thus written in terms of the sum of an infinite number of terms; however, the major contribution to the covariance is due to the term associated with K_0, which accounts for 70% of variance at lag 0 and for nearly 100% of variance at lags $|\tau| > 1$ year. The theoretical prediction shown in Fig. 9a uses 10 terms in Eq. (B.3), while the contributions of higher-order terms are negligible.

The atmospheric autocorrelation function $C_{\mathrm{a,\,c}}$ has two contributions: the one associated with the "uncoupled" part of atmospheric spectrum (17) and the one due to coupling. The former contribution, given in Appendix A, accounts for nearly 100% of covariance at lag 0. To estimate the "coupled" part is completely analogous to the procedure above for oceanic covariance. The integrand in this case decays slower as $R \to \infty$, but still uniformly converges to zero, so the formulas above can be applied directly by using appropriate f and the same g. Unlike for oceanic case, the residue K_0 accounts for majority of covariance only for lags $|\tau| > 7$ years, while for shorter lags the contributions of the terms K_n, $1 \leq n \leq 10$ are all important and lead, in particular, to a step-function-like behavior at lag ± 5 years (see Fig. 9b).

References

Bar-Eli, K. and R. J. Field, 1998. Earth average temperature: A time delay approach. J. Geophys. Res. Atmos., 103(D20), 25,949-25,956.

Battisti D. S., and A. C. Hirst, 1989. Interannual variability in the tropical atmosphere/ocean system: Influence of the basic state, ocean geometry and non-linearity. J. Atmos. Sci., 46,1687–1712.

Berloff, P. S., 2005a. On dynamically consistent eddy fluxes. Dyn. Atmos. Oceans, 38, 123–146.

Berloff, P. S., 2005b. Random-forcing model of the mesoscale ocean eddies. J. Fluid Mech., 529, 71—95.

Berloff, P., 2005c. On rectification of randomly forced flows. J. Mar. Res., 31, 497–527.

Berloff, P. S., W. K. Dewar, S. V. Kravtsov and J. C. McWilliams, 2007. Ocean eddy dynamics in a coupled ocean–atmosphere model. J. Phys. Oceanogr., 37, 1103–1121.

Berner, J., and G. Branstator, 2007. Linear and nonlinear signatures of the planetary wave dynamics of an AGCM: Probability density functions. J. Atmos. Sci., 64, 117–136.

Bhattacharya, K., M. Ghil, and I. L. Vulis, 1982. Internal Variability of an energy-balance model with delayed albedo effects. J. Atmos. Sci., 39, 1747–1773.

Bryan, K. and F. C. Hansen, 1993. A toy model of North Atlantic climate variability on a decade-to-century time scale. In: *The Natural Variability of the Climate System on 10–100 Year Time Scales*. U. S. Natl. Acad. of Sci.

Cessi, P., 1994. A simple box model of stochastically forced thermohaline flow. J. Phys. Oceanogr, 24, 1911–1920.

Cessi, P., 2000. Thermal feedback on wind stress as a contributing cause of climate variability. J. Climate, 13, 232–244.

Churchill, R. V., 1960. *Complex Variables and Applications*. McCraw-Hill, New York, 297pp.

Czaja, A. and Marshall, J., 2001. Observations of atmosphere–ocean coupling in the North Atlantic. Quart. J. Roy. Meteor. Soc., 127, 1893–1916.

Deloncle, A., R. Berk, F. DAndrea, and M. Ghil, 2007. Weather regime prediction using statistical learning. J. Atmos. Sci., 64, 1619–1635.

Deser, C. and Blackmon, M. L., 1993. Surface climate variations over the North Atlantic Ocean during winter: 1900–1989. J. Climate, 6, 1743–1753.

Dewar, W.K., 2001. On ocean dynamics in mid-latitude climate. J. Climate, 14, 4380–4397.

Dewar, W.K., 2003. Nonlinear midlatitude ocean adjustment. J. Phys. Oceanogr., 33, 1057–1081.

Dijkstra, H. A. and M. Ghil, 2005. Low-frequency variability of the large-scale ocean circulation: A dynamical systems approach. Rev. Geophysics, 43, RG3002, doi:10.1029/2002RG000122 (38 pp.).

Feliks, Y., M. Ghil and E. Simonnet, 2004. Low-frequency variability in the midlatitude atmosphere induced by an oceanic thermal front. J. Atmos. Sci., 61, 961–981.

Feliks, Y., M. Ghil and E. Simonnet, 2007. Low-frequency variability in the mid-latitude baroclinic atmosphere induced by an oceanic thermal front. J. Atmos. Sci., 64, 97–116.

Gardiner, C. W., 1985. *Handbook of Stochastic Methods for Physics, Chemistry, and the Natural Sciences*. Springer-Verlag, 442+xix.

Ghil, M. and S. Childress, 1987. *Topics in Geophysical Fluid Dynamics Atmospheric Dynamics, Dynamo Theory and Climate Dynamics*. Springer-

Verlag, New York, 485 pp.

Ghil, M, et al., 2002. Advanced spectral methods for cli- matic time series. Rev. Geophys., 40(1), 3.1–3.41, doi: 10.1029/2000GR000092.

Grötzner, A., M. Latif and T. P. Barnett, 1998. A decadal climate cycle in the North Atlantic Ocean as simulated by ECHO coupled GCM. J. Climate, 11, 831–847.

Hasselmann, K., 1976. Stochastic climate models. Part I: Theory. Tellus, 28, 289–305.

Hsu, C. J., and F. Zwiers, 2001. Climate change in recurrent regimes and modes of Northern Hemisphere atmospheric variability. J. Geophys. Res., 106, 20,145–20,160.

Hurrell, J., 1995. Decadal trends in the North Atlantic Oscillation: Regional temperatures and precipitation. Science, 269, 676–679.

Hurrell, J. W., Y. Kushnir, G. Ottersen and M. Visbeck, 2003. An overview of the North Atlantic Oscillation. Geophys. Monogr., 134, 2217–2231.

Jiang, S., F.-F. Jin and M. Ghil, 1995. Multiple equilibria, periodic, and aperiodic solutions in a wind-driven, double-gyre, shallow-water model. J. Phys. Oceanogr., 25, 764–786.

Jin, F.-F., 1997. A theory of interdecadal climate variability of the North Pacific ocean–atmosphere system. J. Climate, 10, 1821–1835.

Kramers, H. A., 1940. Brownian motion in a field of force and the diffusion model of chemical reactions. Physica, 7, 284–304.

Kravtsov, S., Robertson, A.W. and Ghil, M., 2005a. Bimodal behavior in a baroclinic β-channel model. J. Atmos. Sci., 62, 1746–1769.

Kravtsov, S., Kondrashov, D. and Ghil, M., 2005b. Multiple regression modeling of nonlinear processes: Derivation and applications to climatic variability, 2005b, J. Climate, 18, 4404–4424.

Kravtsov, S., Robertson, A.W. and Ghil, M., 2006a. Multiple regimes and low-frequency oscillations in the Northern Hemisphere's zonal-mean flow. J. Atmos. Sci., 63, 840–860.

Kravtsov, S., Berloff, P., Dewar, W.K., McWilliams, J.C. and Ghil, M., 2006b. Dynamical origin of low-frequency variability in a highly nonlinear mid-latitude coupled model. J. Climate, 19, 6391–6408.

Kravtsov, S., W. K. Dewar, P. Berloff, J. C. McWilliams, and M. Ghil, 2007a: A highly nonlinear coupled mode of decadal variability in a mid-latitude ocean–atmosphere model. Dyn. Atmos. Oceans, 43, 123–150.

Kravtsov, S., W. K. Dewar, P. Berloff, J. C. McWilliams, and M. Ghil, 2007b: Midlatitude coupled climate variability in models and data. Nonlin. Proc. Geophys., submitted.

Kushnir, Y., 1994. Interdecadal variations in North Atlantic sea surface temperature and associated atmospheric conditions. J. Climate, 7, 141–157.

Kushnir, Y. and Held, I., 1996. Equilibrium atmospheric response to North Atlantic SST anomalies. J. Climate, 9, 1208–1220.

Marshall, J., Johnson, H. and Goodman, J., 2000. A study of the interaction of the North Atlantic Oscillation with ocean circulation. J. Climate, 14, 1399–1421.

McDougall, T. J., and W. K. Dewar, 1998. Vertical mixing, cabbeling and thermobaricity in layered models. J. Phys. Oceanogr., 28, 1458–1480.

Mehta, V.M., Suarez, M.J., Manganello, J.V. and Delworth, T.L., 2000. Oceanic influence on the North Atlantic Oscillation and associated Northern Hemisphere climate variations: 1959–1993. Geoph. Res. Letts., 27, 121–124.

Miller, R. N., M. Ghil and F. Gauthiez, 1994. Advanced data assimilation in strongly nonlinear dynamical systems. J. Atmos. Sci., 51, 1037–1056.

Neelin, J.D. and Weng, W., 1999. Analytical prototypes for ocean–atmosphere

interaction at midlatitudes. Coupled feedbacks as a sea surface temperature dependent stochastic process. J. Climate, 12, 697–721.

Otnes, R. and L. Enochson, 1978. *Applied Time Series Analysis*, Vol. I. Wiley and Sons, 449 pp.

Peng, S., L. A. Mysak, H. Ritchie, J. Derome and B Dugas, 1995. The differences between early and middle winter atmospheric response to sea surface temperature anomalies in the northwest Atlantic. J. Climate, 8, 137–157.

Peng, S., W. A. Robinson and M. P. Hoerling, 1997. The modeled atmospheric response to midlatitude SST anomalies and its dependence on background circulation states. J. Climate, 10, 971–987.

Preisendorfer, R. W., 1988. *Principal Component Analysis in Meteorology and Oceanography*. Elsevier, New York, 425pp.

Rodwell, M.J., Rodwell, D.P., and Folland, C.K., 1999. Oceanic forcing of the wintertime North Atlantic Oscillation and European climate. Nature, 398, 320–323.

Saravanan, R. and McWilliams, J.C., 1998. Advective ocean–atmosphere interaction: An analytical stochastic model with implications for decadal variability. J. Climate, 11, 165–188.

Simonnet, E., M. Ghil and H. A. Dijkstra, 2005. Homoclinic bifurcations in the quasi-geostrophic double-gyre circulation. J. Mar. Res., 63, 931–956.

Smyth, P., K. Ide and M. Ghil, 1999. Multiple regimes in Northern Hemisphere height fields via mixture model clustering. J. Atmos. Sci., 56, 3704–3723.

Stephenson, D. B., A. Hannachi, and A. ONeill, 2004. On the existence of multiple climate regimes. Quart. J. Roy. Meteor. Soc., 130, 583–605.

Stommel, H. and W. R. Young, 1993.The average $T - S$ relation of a stochastically forced box model. J. Phys. Oceanogr., 23, 151–158.

Suarez, M. J. and P. S. Schopf, 1988. A delayed action oscillator for ENSO.

J. Atmos. Sci., 45, 3283–3287.

Timmerman, A., M. Latif, R. Voss, and A. Grötzner, 1998. Northern Hemispheric interdecadal variability: A coupled air–sea mode. J. Climate, 11, 1906–1931.

Wax, N., 1954. *Selected Papers on Noise and Stochastic Processes*. Dover, New York, 337pp.

Wunsch, C., 1999. The interpretation of short climate records, with comments on the North Atlantic and Southern Oscillations. Bull. Amer. Meteorol. Soc., 245–255.

Figure Captions

Fig. 1. QG model's atmospheric behavior: (a) Time mean (contours; negative contours dashed, zero contours dotted) and the leading stationary EOF (color levels) of the ocean Ekman pumping w_{E} (10^{-6} m s^{-1}); the latter EOF-3 accounts for 15% of the 30-day low-pass filtered w_{E} variance. (b) Time series of EOF-3.

Fig. 2. QG model's oceanic climatology: (a) Upper-layer transport Ψ_1 (Sv), contour interval $CI = 10$, negative contours dashed, zero contours dotted; heavy solid lines mark the jet-extension subdomain which is studied in more detail in panels (b–d) and in Fig. 3. Panels (b–d) show Ψ_1 [contours, same as in (a)] and time-mean eddy forcing in the upper layer (color levels, Sv month^{-1}) due to: (b) all eddies; (c) LL eddies; and (d) HH eddies, see text for details.

Fig. 3. QG model's oceanic variability. Shown is lagged regression of Ψ_1 (contours; $CI = 2$ Sv, negative contours dashed, zero contours dotted) and ocean eddy forcing (color levels, in Sv month^{-1}) onto 5-year low-pass filtered time series of Ψ_1's EOF-1 (the latter accounts for 28% of total Ψ_1 variance). Columns show forcing due to all eddies (left), LL eddies (middle), and HH eddies (right); see text for details. (a) Lag –10 years; (b) lag –5 years; (c) lag 0; (d) lag +5 years, and (e) lag +10 years.

Fig. 4. Coupled mode in QG model: (a) Spectra of the ocean kinetic energy and atmospheric jet position time series based on an 800-year-long integration of the model. Both time series were annually averaged, centered and normalized by their respective standard deviations prior to the analysis. The spectra were

computed by Welch's method using a window size of 40 years. (b) Squared coherence spectrum of the ocean kinetic energy and atmospheric jet position. The data were processed in the same way as for computing the spectra shown in (a).

Fig. 5. Coupled mode in QG model (continued): (a) Lagged correlation between the time series of annual occurrences of atmospheric low-latitude state and upper ocean heat content annual time series (see text for details). (b) Ocean adjustment to a permanent atmospheric jet shift from the low-latitude to the high-latitude state; normalized time series of the distance between the final and initial zonally averaged SST fields (light solid line). Heavy solid line represents a manual smoothing of the original time series to better visualize different stages of the adjustment process (see text).

Fig. 6. (a) The potential $V(x;\ \pm 1)$ conditioned on two extreme ocean states of the QG model's coupled mode: low-latitude state (light solid line) and high-latitude state (light dashed line). Heavy lines show the potential $V(x;\ \pm 1)$ used in the conceptual model of Eqs. (4)–(6), in which the shape of V is governed by the parameter a: $a = 0.6$ (heavy solid line) and $a = 0.05$ (heavy dashed line). The quantity x assumes values from the centered, normalized atmospheric jet-position time series. (b) The same as in (a), except that the light lines show the potentials computed by the same procedure as for the QG model time series, but applied to the signal produced by the coupled conceptual model. This signal's "oceanic" component was contaminated by the red noise to mimic the processes absent from the conceptual model.

Fig. 7. Behavior of a conceptual one-variable, one-parameter atmospheric model given by Eqs. (4)–(7). (a) Probability density function (PDF) for $a =$

0.6 (heavy solid line) and $a = 0.05$ (heavy dashed line). (b) Spectra for $a = 0.6$ (light solid line) and $a = 0.6$ (light dashed line); heavy solid and dashed lines show corresponding spectral fits associated with the superposition of random telegraph and Ornstein-Uhlenbeck processes (see text for details).

Fig. 8. Fourier spectra based on a 4000-year-long simulation of a conceptual coupled model (4–7) [light solid lines] along with the associated 95% confidence intervals (light dashed lines), and the theoretical spectra of their simplified counterparts (14–15) [heavy solid lines].

Fig. 9. Autocorrelation function of: (a) ocean variable; (b) atmospheric variable. The estimates are based on: simulation of the conceptual model (4–7) [solid lines]; and theoretical prediction from a simplified conceptual model (14, 15) [dashed lines].

Fig. 10. Same as in Fig. 9, but for the QG model variables: (a) oceanic kinetic energy; (b) atmospheric jet position. Annual time series were used.

Fig. 11. Sensitivity of a simplified conceptual model's (14, 15) ocean-variable (heavy lines) and atmospheric-variable (light lines) spectra to coupling parameter D: (a) $D = 0.01$; (b) $D = 0.05$; (c) $D = 0.1$ (control case); (d) $D = 0.15$. In each panel, dashed lines represent the corresponding uncoupled spectra ($D = 0$).

Fig. 12. Sensitivity of a simplified conceptual model's (14, 15) spectra to ocean damping parameter λ: (a) $\lambda = 0.5$ year^{-1} (control case); (b) $\lambda = 1.5$ year^{-1}; (c) $\lambda = 2.5$ year^{-1}; (d) $\lambda = 3.5$ year^{-1}. Same symbols and conventions as in Fig. 11.

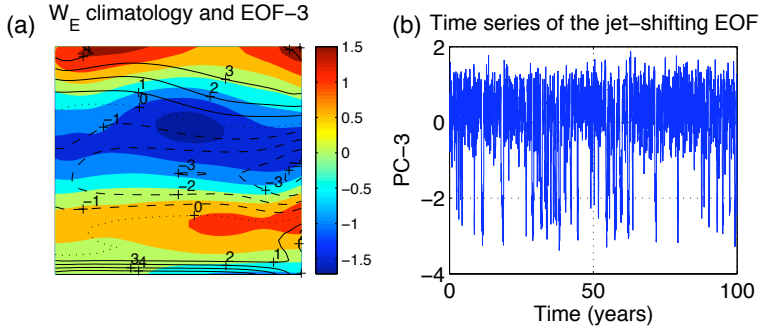

Fig. 1. QG model's atmospheric behavior: (a) Time mean (contours; negative contours dashed, zero contours dotted) and the leading stationary EOF (color levels) of the ocean Ekman pumping w_{E} (10^{-6} m s^{-1}); the latter EOF-3 accounts for 15% of the 30-day low-pass filtered w_{E} variance. (b) Time series of EOF-3.

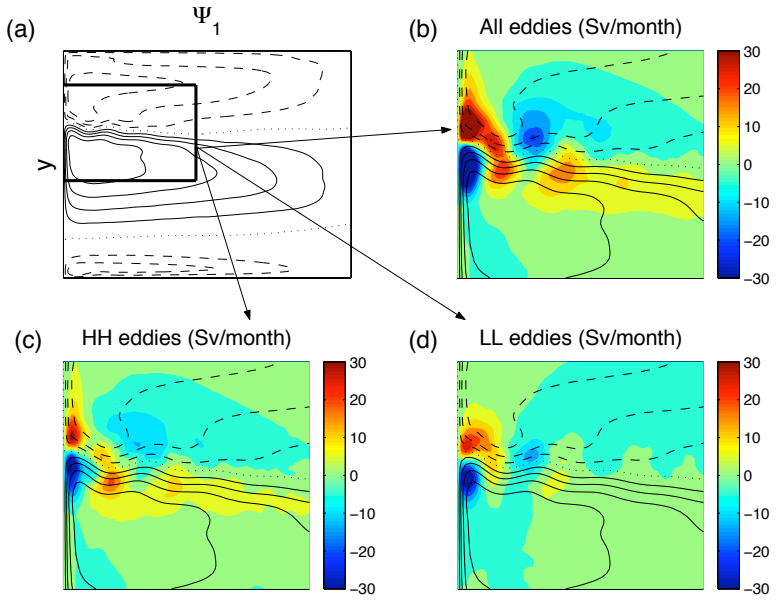

Fig. 2. QG model's oceanic climatology: (a) Upper-layer transport Ψ_1 (Sv), contour interval $CI = 10$, negative contours dashed, zero contours dotted; heavy solid lines mark the jet-extension subdomain which is studied in more detail in panels (b–d) and in Fig. 3. Panels (b–d) show Ψ_1 [contours, same as in (a)] and time-mean eddy forcing in the upper layer (color levels, Sv month^{-1}) due to: (b) all eddies; (c) LL eddies; and (d) HH eddies, see text for details.

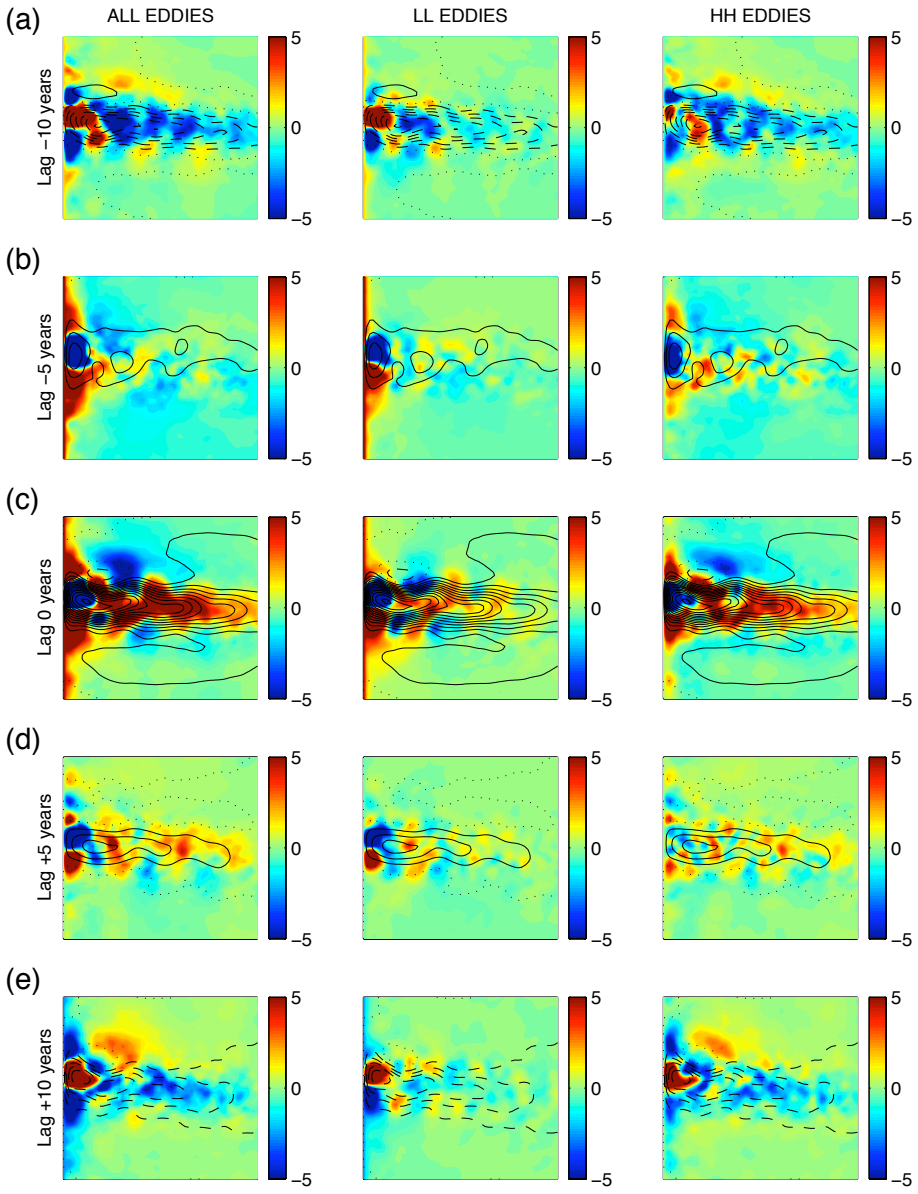

Fig. 3. QG model's oceanic variability. Shown is lagged regression of Ψ_1 (contours; $CI = 2$ Sv, negative contours dashed, zero contours dotted) and ocean eddy forcing (color levels, in Sv month^{-1}) onto 5-year low-pass filtered time series of Ψ_1's EOF-1 (the latter accounts for 28% of total Ψ_1 variance). Columns show forcing due to all eddies (left), LL eddies (middle), and HH eddies (right); see text for details. (a) Lag –10 years; (b) lag –5 years; (c) lag 0; (d) lag +5 years, and (e) lag +10 years.

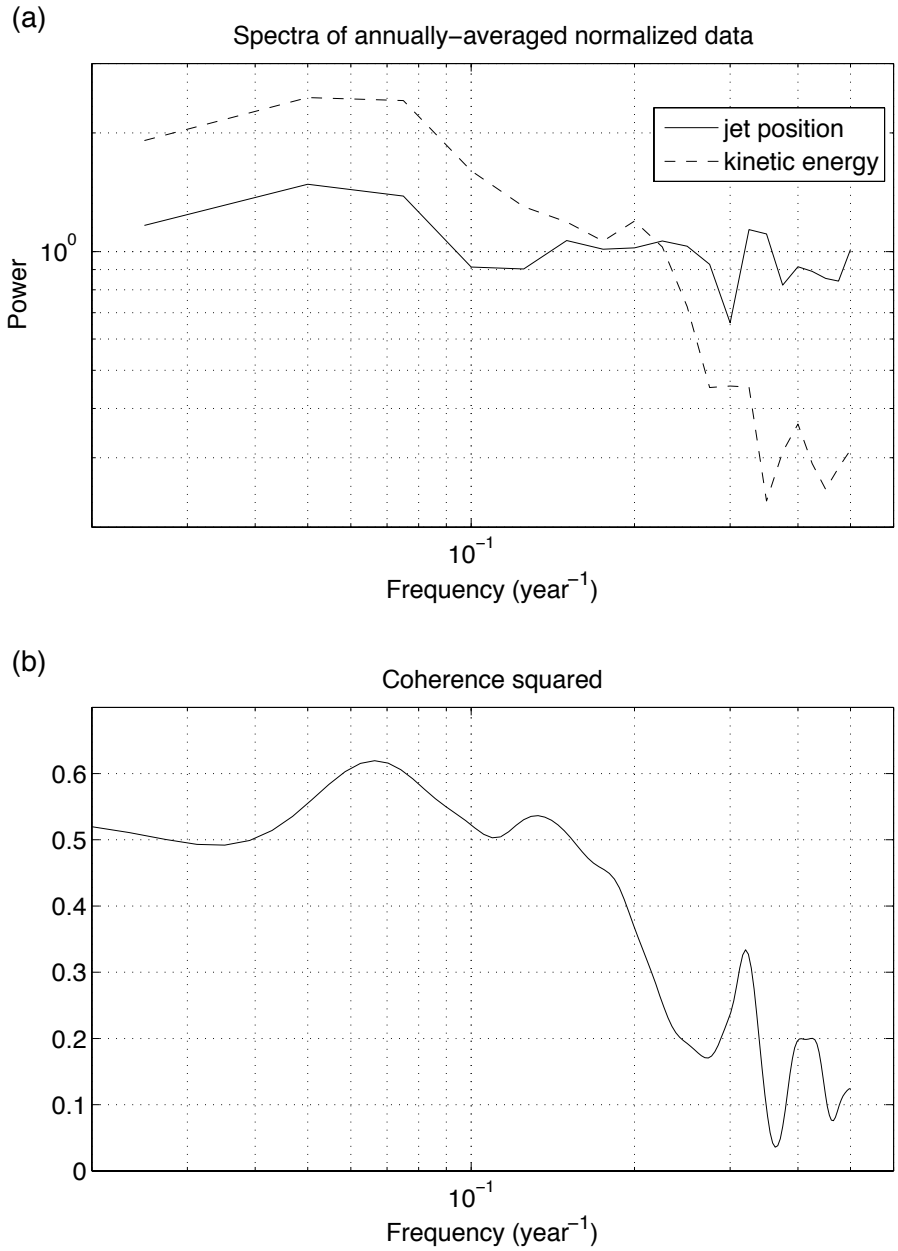

Fig. 4. Coupled mode in QG model: (a) Spectra of the ocean kinetic energy and atmospheric jet position time series based on an 800-year-long integration of the model. Both time series were annually averaged, centered and normalized by their respective standard deviations prior to the analysis. The spectra were computed by Welch's method using a window size of 40 years. (b) Squared coherence spectrum of the ocean kinetic energy and atmospheric jet position. The data were processed in the same way as for computing the spectra shown in (a).

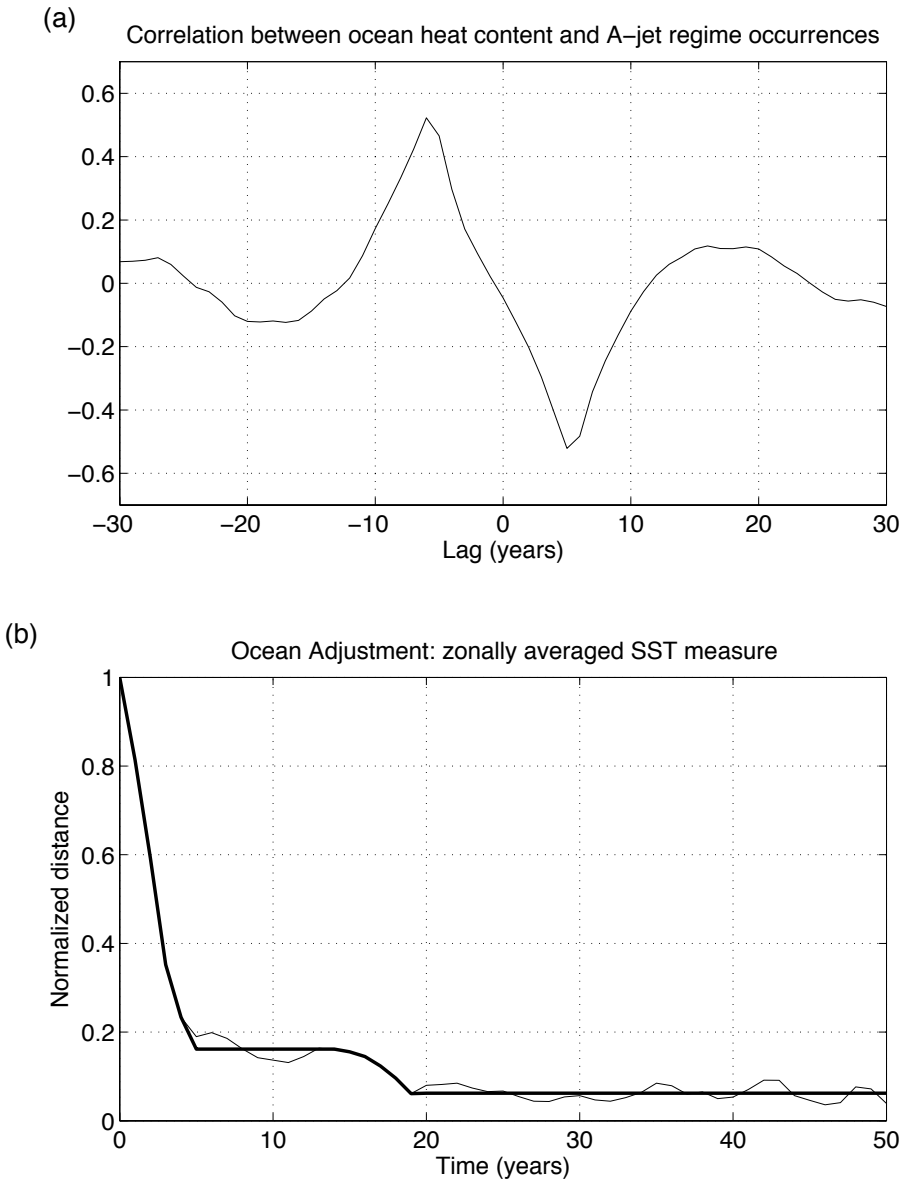

Fig. 5. Coupled mode in QG model (continued): (a) Lagged correlation between the time series of annual occurrences of atmospheric low-latitude state and upper ocean heat content annual time series (see text for details). (b) Ocean adjustment to a permanent atmospheric jet shift from the low-latitude to the high-latitude state; normalized time series of the distance between the final and initial zonally averaged SST fields (light solid line). Heavy solid line represents a manual smoothing of the original time series to better visualize different stages of the adjustment process (see text).

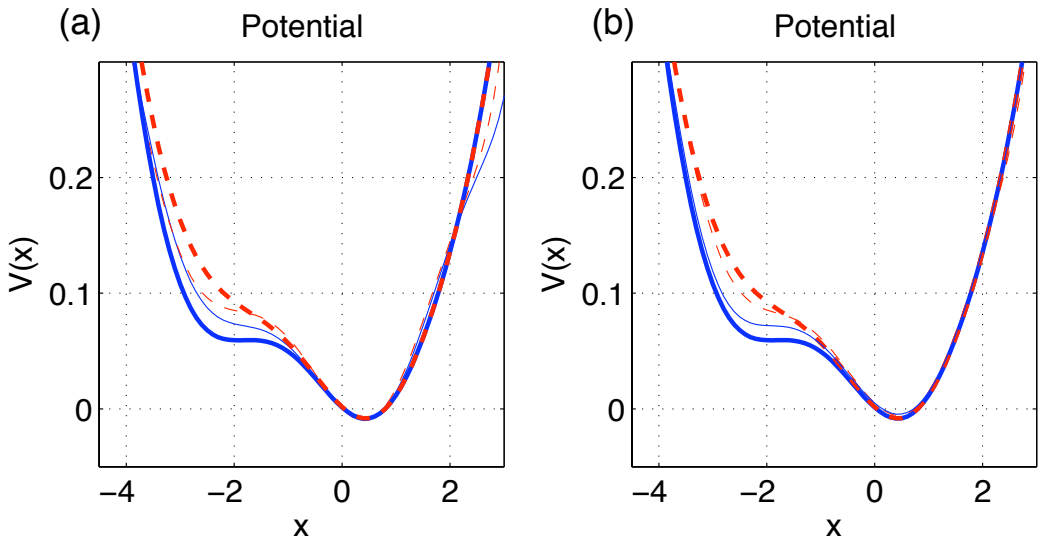

Fig. 6. (a) The potential $V(x;\ \pm 1)$ conditioned on two extreme ocean states of the QG model's coupled mode: low-latitude state (light solid line) and high-latitude state (light dashed line). Heavy lines show the potential $V(x;\ \pm 1)$ used in the conceptual model of Eqs. (4)–(6), in which the shape of V is governed by the parameter a: $a = 0.6$ (heavy solid line) and $a = 0.05$ (heavy dashed line). The quantity x assumes values from the centered, normalized atmospheric jet-position time series. (b) The same as in (a), except that the light lines show the potentials computed by the same procedure as for the QG model time series, but applied to the signal produced by the coupled conceptual model. This signal's "oceanic" component was contaminated by the red noise to mimic the processes absent from the conceptual model.

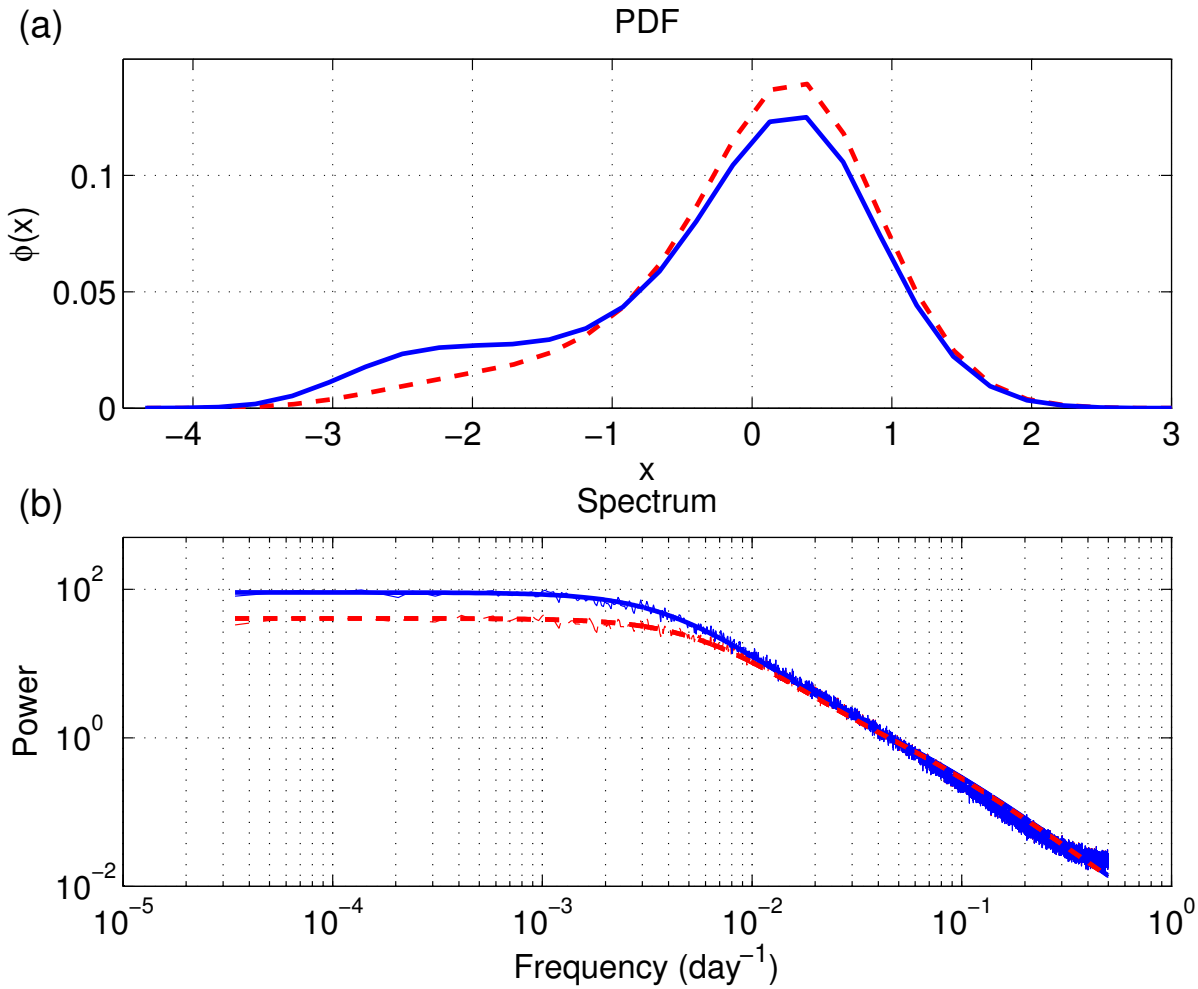

Fig. 7. Behavior of a conceptual one-variable, one-parameter atmospheric model given by Eqs. (4)–(7). (a) Probability density function (PDF) for $a = 0.6$ (heavy solid line) and $a = 0.05$ (heavy dashed line). (b) Spectra for $a = 0.6$ (light solid line) and $a = 0.6$ (light dashed line); heavy solid and dashed lines show corresponding spectral fits associated with the superposition of random telegraph and Ornstein-Uhlenbeck processes (see text for details).

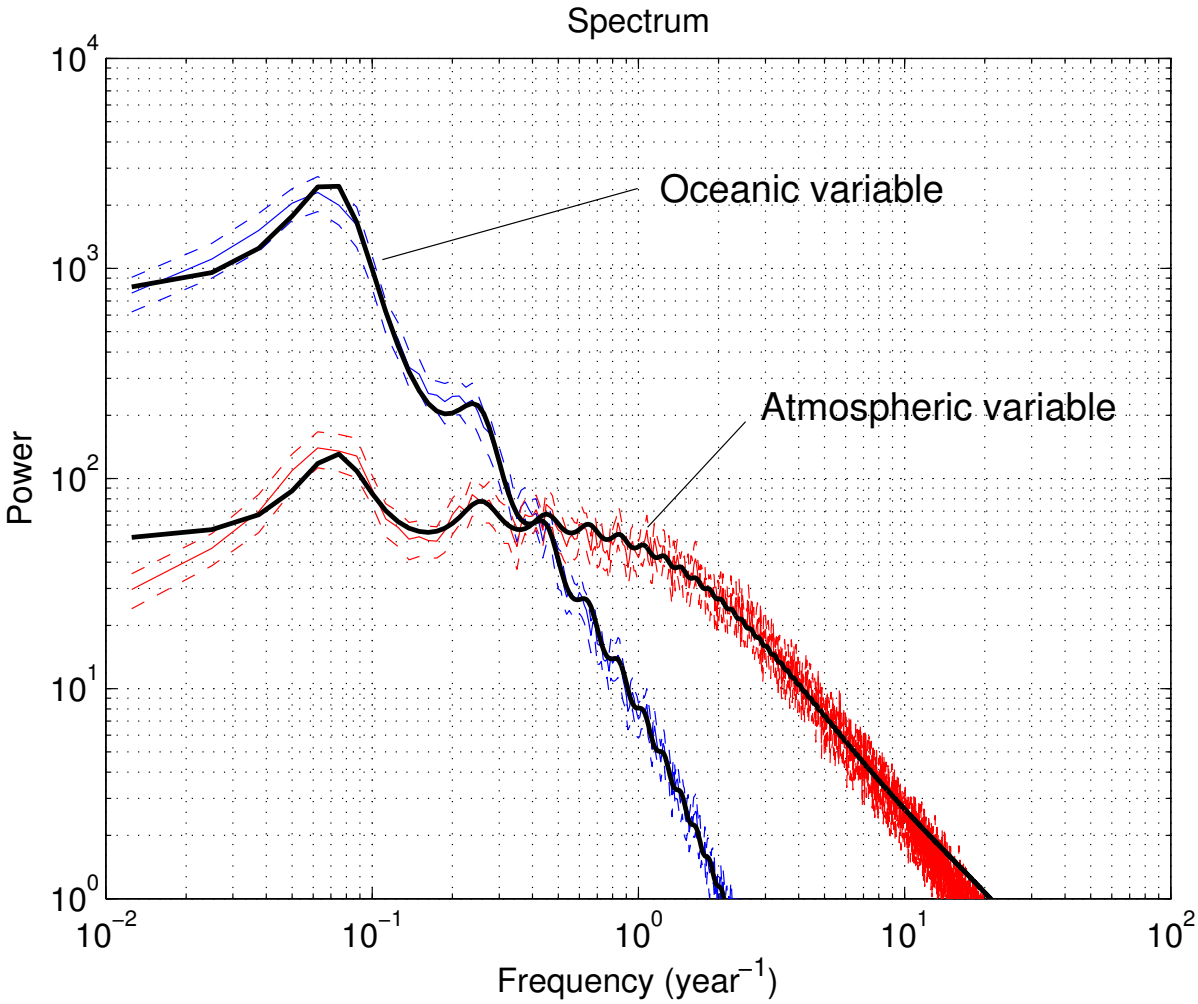

Fig. 8. Fourier spectra based on a 4000-year-long simulation of a conceptual coupled model (4–7) [light solid lines] along with the associated 95% confidence intervals (light dashed lines), and the theoretical spectra of their simplified counterparts (14, 15) [heavy solid lines].

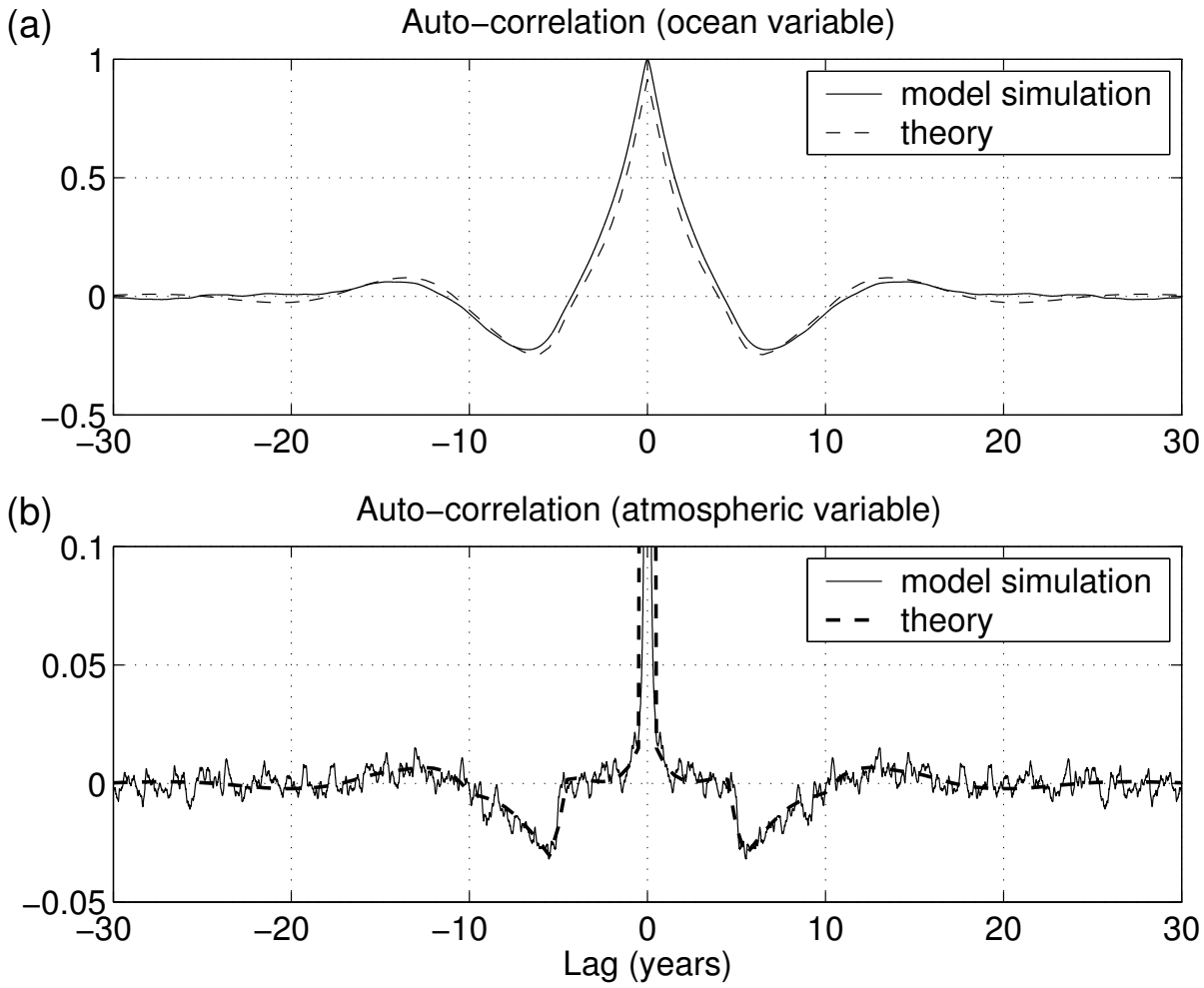

Fig. 9. Autocorrelation function of: (a) ocean variable; (b) atmospheric variable. The estimates are based on: simulation of the conceptual model (4–7) [solid lines]; and theoretical prediction from a simplified conceptual model (14, 15) [dashed lines].

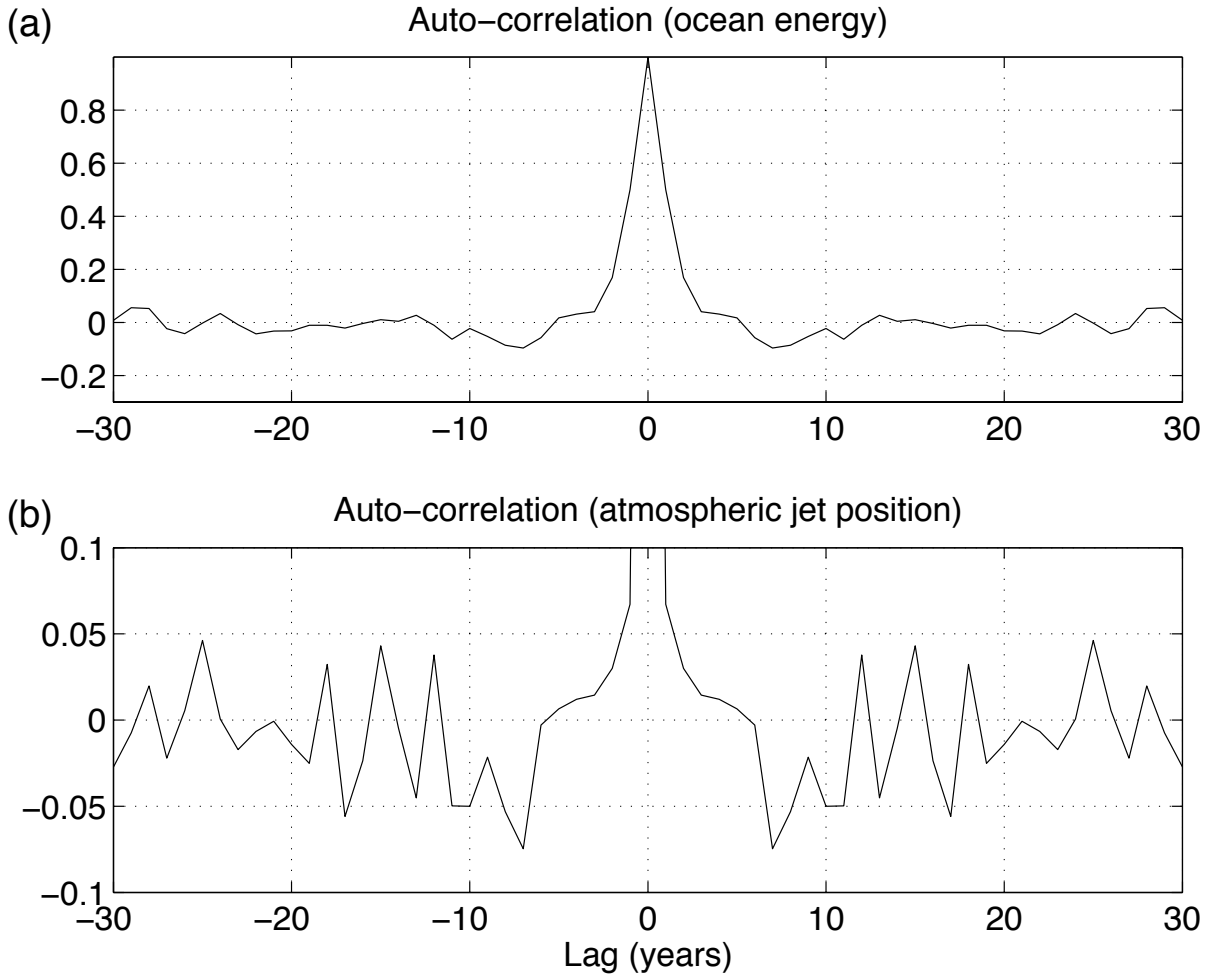

Fig. 10. Same as in Fig. 9, but for the QG model variables: (a) oceanic kinetic energy; (b) atmospheric jet position. Annual time series were used.

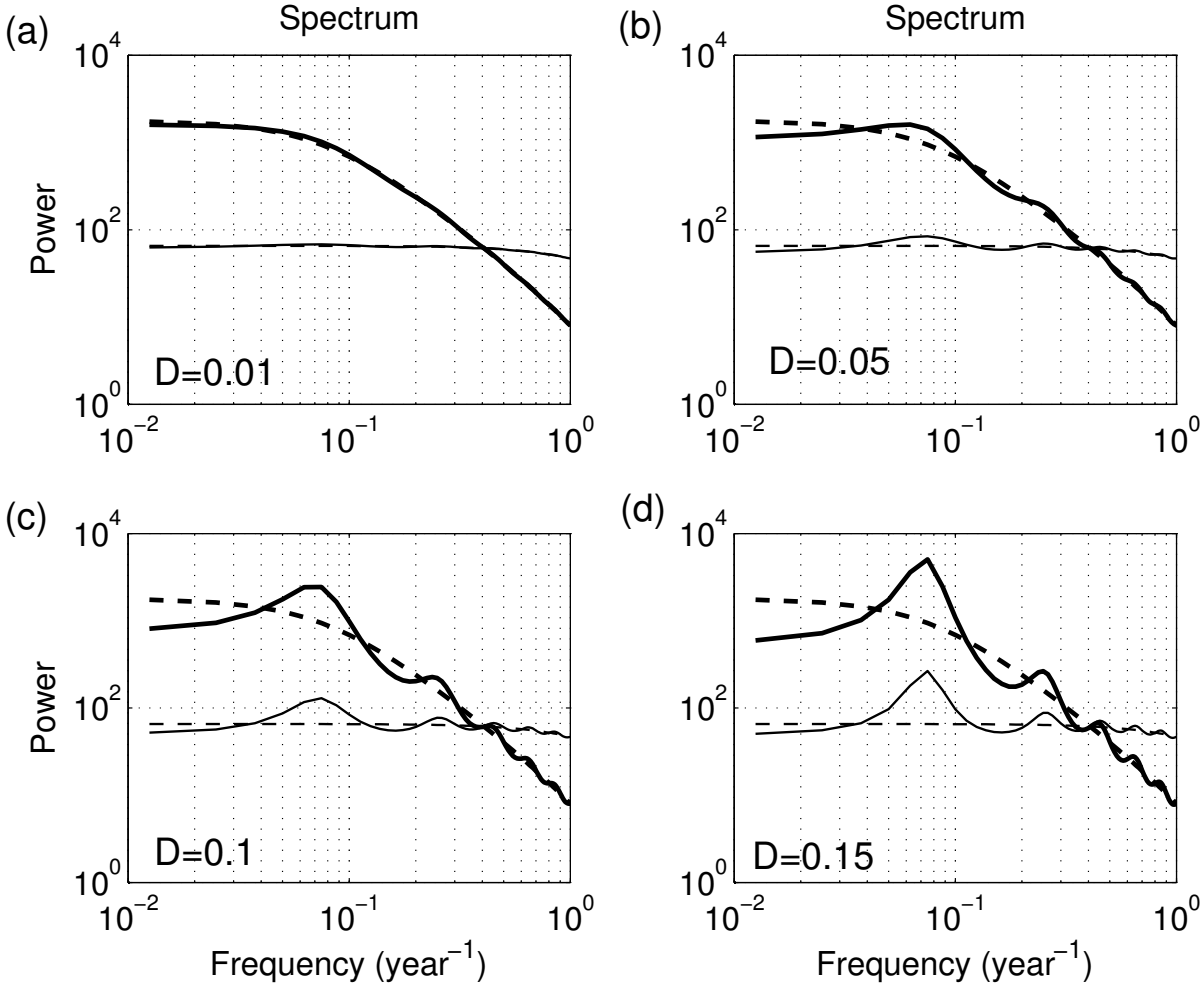

Fig. 11. Sensitivity of a simplified conceptual model's (14, 15) ocean-variable (heavy lines) and atmospheric-variable (light lines) spectra to coupling parameter D: (a) $D = 0.01$; (b) $D = 0.05$; (c) $D = 0.1$ (control case); (d) $D = 0.15$. In each panel, dashed lines represent the corresponding uncoupled spectra ($D = 0$).

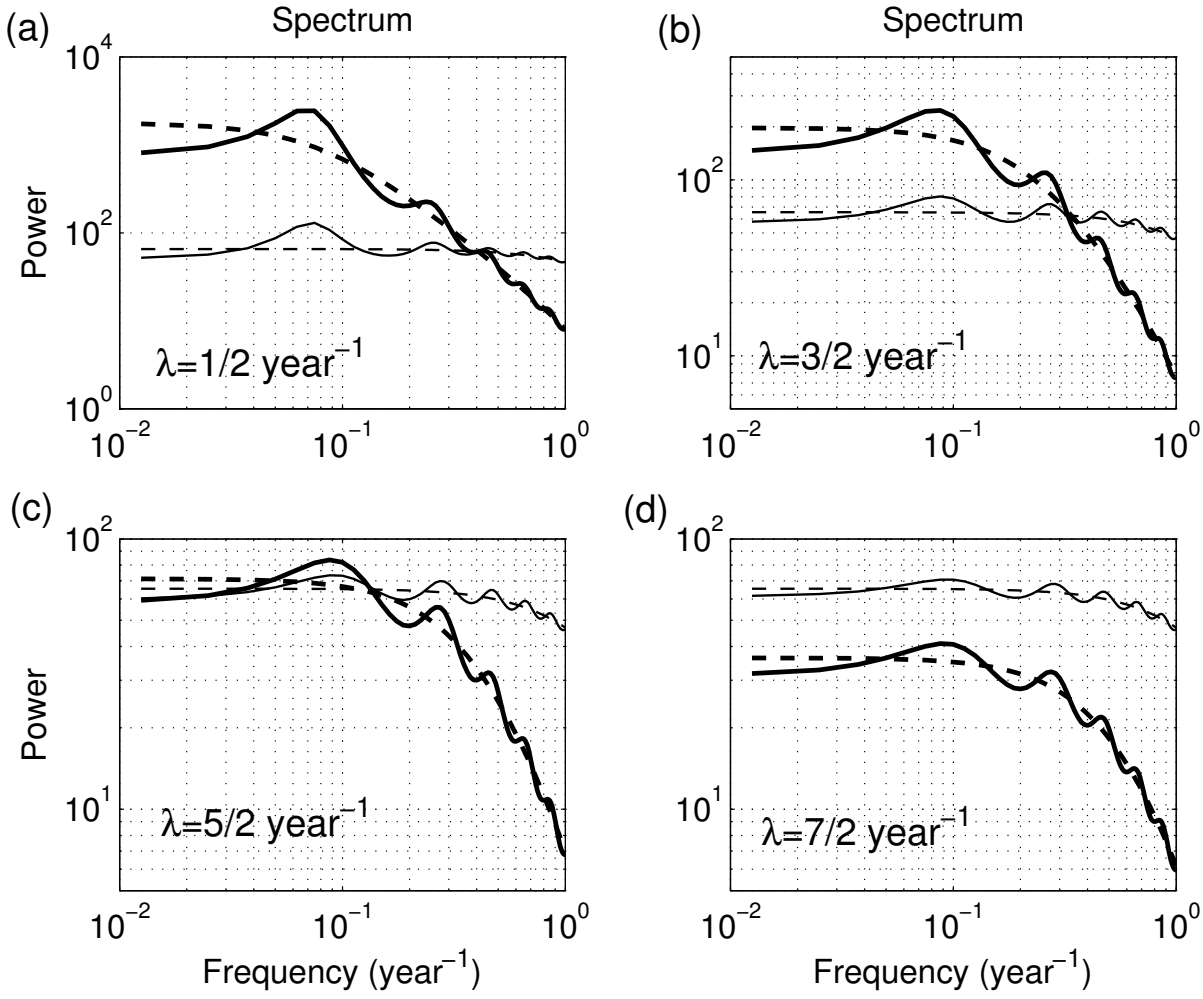

Fig. 12. Sensitivity of a simplified conceptual model's (14, 15) spectra to ocean damping parameter λ: (a) $\lambda = 0.5$ year^{-1} (control case); (b) $\lambda = 1.5$ year^{-1}; (c) $\lambda = 2.5$ year^{-1}; (d) $\lambda = 3.5$ year^{-1}. Same symbols and conventions as in Fig. 11.